AGU PUBLICATIONS

JGR

Journal of Geophysical Research: Solid Earth

RESEARCH ARTICLE
10.1002/2017JB013987

Key Points:
- Jurassic to Paleogene Himalayan carbonates are pervasively remagnetized by oxidation of diagenetic iron sulfide to fine-grained magnetite
- Lower Cretaceous volcaniclastic rocks retain a primary remanence
- Thorough rock magnetic and petrographic information are more reliable criteria for diagnosing remagnetization in carbonates than filed tests

Supporting Information:
- Supporting Information S1

Correspondence to:
W. Huang,
wentaohuang@email.arizona.edu

Citation:
Huang, W., P. C. Lippert, Y. Zhang, M. J. Jackson, M. J. Dekkers, J. Li, X. Hu, B. Zhang, Z. Guo, and D. J. J. van Hinsbergen (2017), Remagnetization of carbonate rocks in southern Tibet: Perspectives from rock magnetic and petrographic investigations, *J. Geophys. Res. Solid Earth*, *122*, doi:10.1002/2017JB013987.

Received 14 JAN 2017
Accepted 16 MAR 2017
Accepted article online 20 MAR 2017

Remagnetization of carbonate rocks in southern Tibet: Perspectives from rock magnetic and petrographic investigations

Wentao Huang[1,2,3], Peter C. Lippert[3], Yang Zhang[1], Michael J. Jackson[4], Mark J. Dekkers[5], Juan Li[6], Xiumian Hu[6], Bo Zhang[1], Zhaojie Guo[1], and Douwe J. J. van Hinsbergen[5]

[1]Key Laboratory of Orogenic Belts and Crustal Evolution, Ministry of Education, School of Earth and Space Sciences, Peking University, Beijing, China, [2]Department of Geosciences, University of Arizona, Tucson, Arizona, USA, [3]Department of Geology and Geophysics, University of Utah, Salt Lake City, Utah, USA, [4]Institute for Rock Magnetism, Department of Earth Sciences, University of Minnesota, Twin Cities, Minneapolis, Minnesota, USA, [5]Department of Earth Sciences, Utrecht University, Utrecht, Netherlands, [6]School of Earth Sciences and Engineering, Nanjing University, Nanjing, China

Abstract The latitudinal motion of the Tibetan Himalaya—the northernmost continental unit of the Indian plate—is a key component in testing paleogeographic reconstructions of the Indian plate before the India-Asia collision. Paleomagnetic studies of sedimentary rocks (mostly carbonate rocks) from the Tibetan Himalaya are complicated by potentially pervasive yet cryptic remagnetization. Although traditional paleomagnetic field tests reveal some of this remagnetization, secondary remanence acquired prior to folding or tilting easily escapes detection. Here we describe comprehensive rock magnetic and petrographic investigations of Jurassic to Paleocene carbonate and volcaniclastic rocks from Tibetan Himalayan strata (Tingri and Gamba areas). These units have been the focus of several key paleomagnetic studies for Greater Indian paleogeography. Our results reveal that while the dominant magnetic carrier in both carbonate and volcaniclastic rocks is magnetite, their magnetic and petrographic characteristics are distinctly different. Carbonate rocks have "wasp-waisted" hysteresis loops, suppressed Verwey transitions, extremely fine grain sizes (superparamagnetic), and strong frequency-dependent magnetic susceptibility. Volcaniclastic rocks exhibit "pot-bellied" hysteresis loops and distinct Verwey transitions. Electron microscopy reveals that magnetite grains in carbonate rocks are pseudomorphs of early diagenetic pyrite, whereas detrital magnetite is abundant and pyrite is rarely oxidized in the volcaniclastic rocks. We suggest that the volcaniclastic rocks retain a primary remanence, but oxidation of early diagenetic iron sulfide to fine-grained magnetite has likely caused widespread chemical remagnetization of the carbonate units. We recommend that thorough rock magnetic and petrographic investigations are prerequisites for paleomagnetic studies throughout southern Tibet and everywhere in general.

1. Introduction

Quantitative paleogeographic reconstructions are best constrained if they are based on marine magnetic anomalies and fracture zones in the world's oceans, but where continent-derived terranes are presently surrounded by sutures and/or fold-thrust belts, quantification of their past plate motion relies heavily on paleomagnetic observation. For example, Indian Ocean reconstructions show that the Indian plate was once part of east Gondwana, but rifted from Gondwana during the Early Cretaceous, and after Late Cretaceous to Paleogene northward drift, it collided with the southernmost margin of Asia to form the Himalayan fold-thrust belt and contribute to the crustal thickening of the Tibetan Plateau in Cenozoic (Figure 1a) [e.g., *Klootwijk*, 1984; *Garzanti*, 1999; *Yin and Harrison*, 2000; *van Hinsbergen et al.*, 2011]. Within the Himalaya, however, continent-derived rock units exist that are at present surrounded by major thrusts (Figure 1b) and that therefore have a motion history relative to both Eurasia and India. To quantify that motion history, paleomagnetic investigations of the Tibetan Himalaya (TH), which represents the northernmost continental crust derived from the Indian plate [e.g., *Powell and Conaghan*, 1973; *Hodges*, 2000], have focused on Mesozoic and Cenozoic strata. The paleolatitudes calculated from these studies are then compared to the paleolatitudes of the Indian continent (derived from a Global Apparent Polar Wander Path) [e.g., *Torsvik et al.*, 2012] and constrain the dimension of "Greater India" (defined as the retrodeformed area between the former northern margin of the TH and the modern southernmost thrust of

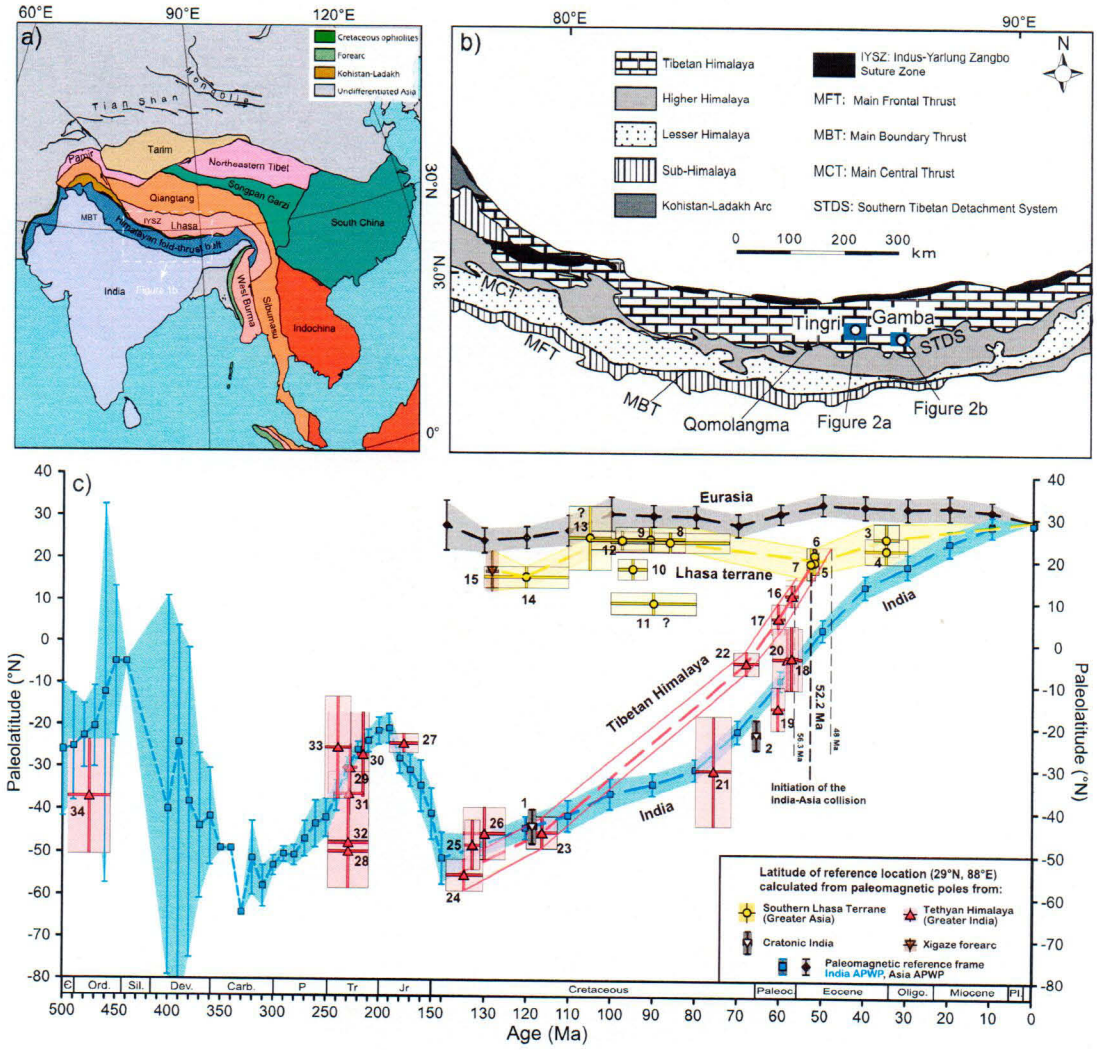

Figure 1. (a) Tectonic map of the India-Asia collision zone (modified from *Huang et al.* [2015d]). (b) Simplified geologic map of the Himalaya, modified from *Li et al.* [2015]. (c) Paleolatitudes of a reference site (29°N, 88°E) in Eurasian, Greater Asian, Tibetan Himalayan, and Indian reference frames, modified from *van Hinsbergen et al.* [2012], *Lippert et al.* [2014], and *Hu et al.* [2016a]. Numbers correspond to paleomagnetic poles described and listed in Table S1 with references in *Hu et al.* [2016a]. Poles 1 and 2 are determined from lavas in cratonic India, poles 3–15 are determined from volcanic and clastic rocks from the Qiangtang and Lhasa terranes, and Xigaze fore arc. Poles 16–22 and 27 of the Tibetan Himalaya (TH) are determined from remagnetized carbonate rocks. The reliability of the Triassic poles 28–33 from the TH, which are also determined from carbonate rocks, should be reevaluated by future studies. Poles 16, 17, and 22 were mistakenly used to constrain the size of Greater India and initiation of the India-Asia collision and as discussed here and in *Huang et al.* [2017].

the Himalaya) through time (Figure 1c) [e.g., *van Hinsbergen et al.*, 2012; *Huang et al.*, 2015d]. Most of these paleomagnetic studies targeted the widespread Tibetan Himalayan carbonate rocks (poles 16–22 and 27–33 in Figure 1c and Table S1 in the supporting information) [*Klootwijk and Bingham*, 1980; *Klootwijk et al.*, 1983; *Besse et al.*, 1984; *Appel et al.*, 1991, 1998; *Patzelt et al.*, 1996; *Schill et al.*, 2002; *Crouzet et al.*, 2003; *Tong et al.*, 2008; *Yi et al.*, 2011; *Ran et al.*, 2012; *Liebke et al.*, 2013; *Huang et al.*, 2015c], except for a few poles calculated from Lower Cretaceous volcaniclastic sandstones and coeval lavas (poles 23–26 in Figure 1c) [*Klootwijk and Bingham*, 1980; *Huang et al.*, 2015c; *Yang et al.*, 2015; *Ma et al.*, 2016] and Ordovician red beds (pole 34 in Figure 1c) [*Torsvik et al.*, 2009]. However, in addition to the potential shallowing of the inclination induced by compaction [*Kodama*, 2012], carbonate rocks are notorious for suffering from pervasive remagnetization which can be at times cryptic and difficult to recognize even with rigorous paleomagnetic field tests [*McCabe et al.*, 1983; *Jackson*, 1990; *Dekkers*, 2012; *van der Voo and Torsvik*, 2012].

Of particular concern, rocks so far studied in the Himalaya rarely record a primary remanent magnetization (NRM). Secondary magnetizations residing in pyrrhotite have been obtained from low-grade metamorphic rocks (mostly metacarbonate rocks); these data have been used to assess tectonic deformation and final thrusting-related thermotectonic processes across the Himalaya [*Appel et al.*, 2012, and references therein]. Secondary NRMs residing in magnetite have also been recently identified from unmetamorphosed Jurassic and Paleogene Tibetan Himalayan carbonate rocks (poles 16, 17, 20, and 27 in Figure 1c) [*Liebke et al.*, 2013; *Huang et al.*, 2015c, 2017]. Consequently, paleogeographic implications of the paleomagnetic data from the TH can be misinterpreted when remagnetized rocks are assumed to carry a primary NRM (poles 16–22 in Figure 1c) [*Besse et al.*, 1984; *Patzelt et al.*, 1996; *Appel et al.*, 1998; *Tong et al.*, 2008; *Yi et al.*, 2011]. Remagnetization residing in secondary magnetite is particularly insidious because it can occur prefolding (pole 27 in Figure 1c) [*Huang et al.*, 2015c], synfolding (poles 16 and 17 in Figure 1c) [*Huang et al.*, 2017], or postfolding (pole 20 in Figure 1c) [*Liebke et al.*, 2013]. Traditional paleomagnetic field tests (the fold test, reversals test, conglomerate test, and baked contact test), even when available, can thus provide only a loose constraint on the origin of the NRM and may not reveal remagnetization at all. Therefore, rigorous criteria independent from paleomagnetic directional information are required for diagnosing remagnetization of carbonate rocks not only in Himalayas but also in orogens worldwide.

In conjunction with our recent work on Paleogene carbonate rocks in the Gamba area [*Huang et al.*, 2017], here we present results from our study of 65 specimens from Jurassic to Paleogene carbonate and volcaniclastic strata of the TH in the Tingri area. We also report results from seven new specimens from Upper Cretaceous carbonate strata in the Gamba area. Specifically, we use high-temperature thermomagnetic experiments, room temperature hysteresis measurements, and low-temperature magnetic experiments to reveal the nature and characteristics of the NRM. We supplement these magnetic measurements with scanning electron microscopy (SEM) and energy-dispersive X-ray spectrometry (EDS) to visually and chemically characterize the magnetic minerals and test our rock magnetic interpretations. We use these observations to compare the rock magnetic and petrographic characteristics of the carbonate rocks to those of the volcaniclastic rocks. Acquisition mechanisms of the NRM carried by Tibetan Himalayan carbonate and volcaniclastic rocks are discussed. Most importantly, we propose rock magnetic and petrographic criteria, which are completely independent from paleomagnetic directions, to evaluate the origin of NRM retained in Tibetan Himalayan rock sequences, criteria that can be easily exported to other orogens.

2. Geological Background and Sampling

The Mesozoic and Cenozoic Tibetan Himalayan sedimentary successions, characterized by passive margin deposits, are well exposed in the Tingri and Gamba areas in southern Tibet (Figure 1b). Detailed stratigraphic descriptions of the sections can be found in Text S1 in the supporting information [e.g., *Willems et al.*, 1996; *Jadoul et al.*, 1998; *Wan et al.*, 2002; *Zhu et al.*, 2005; *Wendler et al.*, 2009; *Hu et al.*, 2010, 2012; *Najman et al.*, 2010; *Li and Hu*, 2013; *Du et al.*, 2015; *Han et al.*, 2016]. We collected 50 carbonate specimens from Jurassic to Paleogene strata in four sections (I–IV) located at 28.48°N/87.04°E, 28.71°N/86.72°E, 28.69°N/86.71°E, and 28.68°N/86.73°E in the Tingri area (Figure 2a). We also collected 15 volcaniclastic specimens from the Lower Cretaceous Wölong Formation in Section I (Figure 2a). In addition to our recent work on Paleogene carbonate rocks in the Gamba area [*Huang et al.*, 2017], we also collected seven carbonate specimens from the uppermost Cretaceous strata in Section V located at 28.28°N/88.52°E near Gamba county (Figure 2b). The Jurassic carbonate and Lower Cretaceous volcaniclastic sandstones in Section I were used to determine poles 27 and 24 (Figure 1c), respectively [*Huang et al.*, 2015c]. The coeval Campanian carbonate rocks which are ~20 km away from Section III were used to determine pole 21 [*Appel et al.*, 1998]. The Zongshan carbonate rocks in Section V were used to determined pole 22 [*Patzelt et al.*, 1996]. Poles 18–20 were determined from Paleogene carbonate rocks in Section IV and nearby region in the Tingri area [*Besse et al.*, 1984; *Tong et al.*, 2008; *Liebke et al.*, 2013]. Poles 16 and 17 were determined from Paleogene carbonate rocks near Gamba county [*Patzelt et al.*, 1996; *Yi et al.*, 2011].

3. Rock Magnetism

Rock magnetic analyses were conducted at the Institute for Rock Magnetism at the University of Minnesota (USA) and the Utah Paleomagnetic Center at the University of Utah (USA). Descriptions of

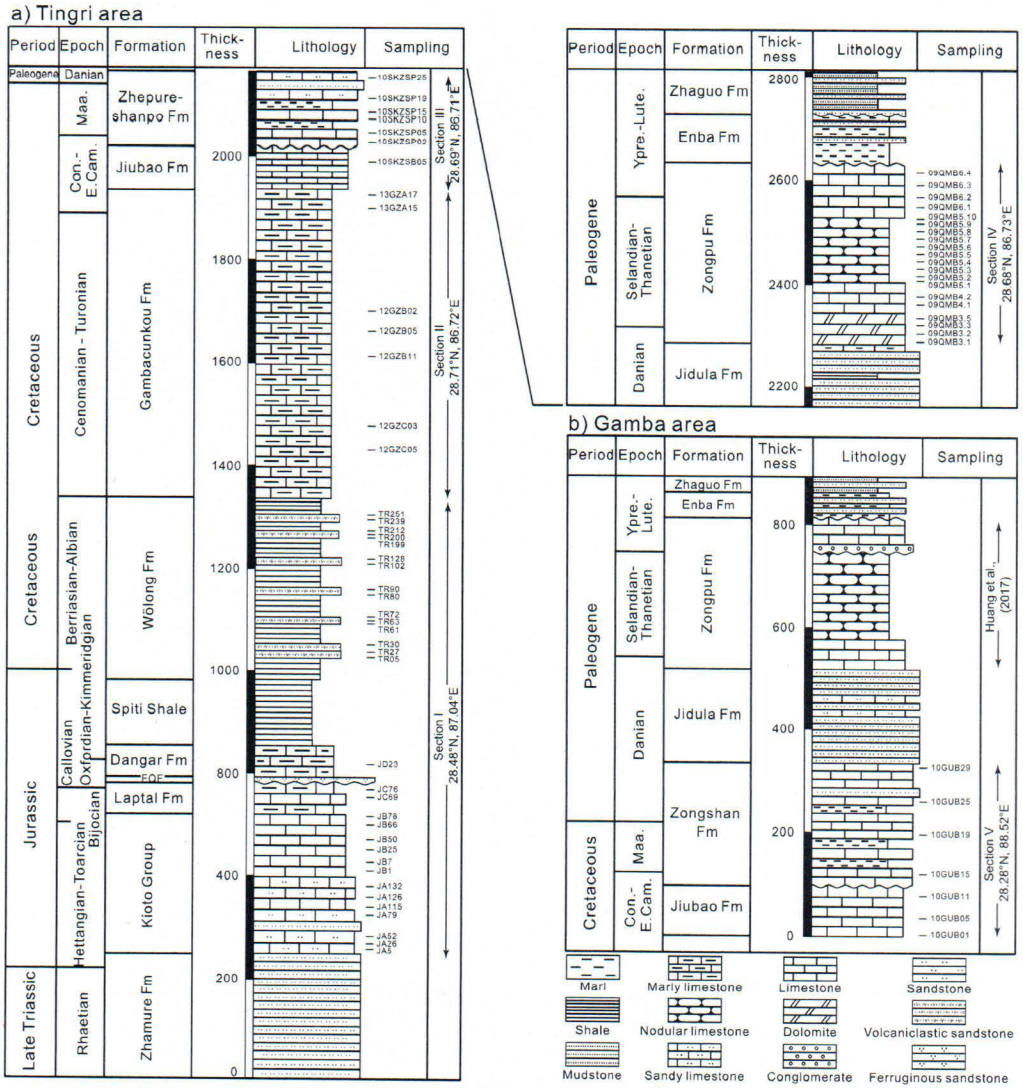

Figure 2. Lithostratigraphy of the Jurassic-Lower Paleogene and uppermost Cretaceous-Lower Paleogene Tibetan Himalayan strata in the (a) Tingri and (b) Gamba areas with the sampling levels indicated.

the methods used for these analyses and of the analyzed specimens are provided in Text S2 in the supporting information.

3.1. Thermomagnetic Runs

High-temperature susceptibility measurements on most carbonate specimens from the Tingri and Gamba areas are characterized by a decrease of susceptibility before 400°C followed by an increase in susceptibility in the temperature range of 420–500°C (Figures 3 and 4d). We attribute this behavior to the formation of new magnetite by oxidation of pyrite [*Zegers et al.*, 2003]. All of the specimens show a sharp decrease in magnetization with increasing temperature up to 580°C (Figures 3 and 4a–4d). The Curie temperatures determined from the first derivative of the measured data ranged from 550 to 580°C, indicating the presence of magnetite [*Dunlop and Ödemir*, 1997]. Additional loss of susceptibility was also observed in some specimens with increasing temperature up to 650°C (Figures 3a–3g, 3j, and 3n), indicating the minor presence of hematite [*Dunlop and Ödemir*, 1997]. The hematite interpretation (or maghemite) is supported by the observation of the Morin transition in low-temperature measurements (see section 3.3.2). The cooling curves for all specimens show a large increase in susceptibility (Figures 3, 4a, and 4c), which we interpret as a consequence

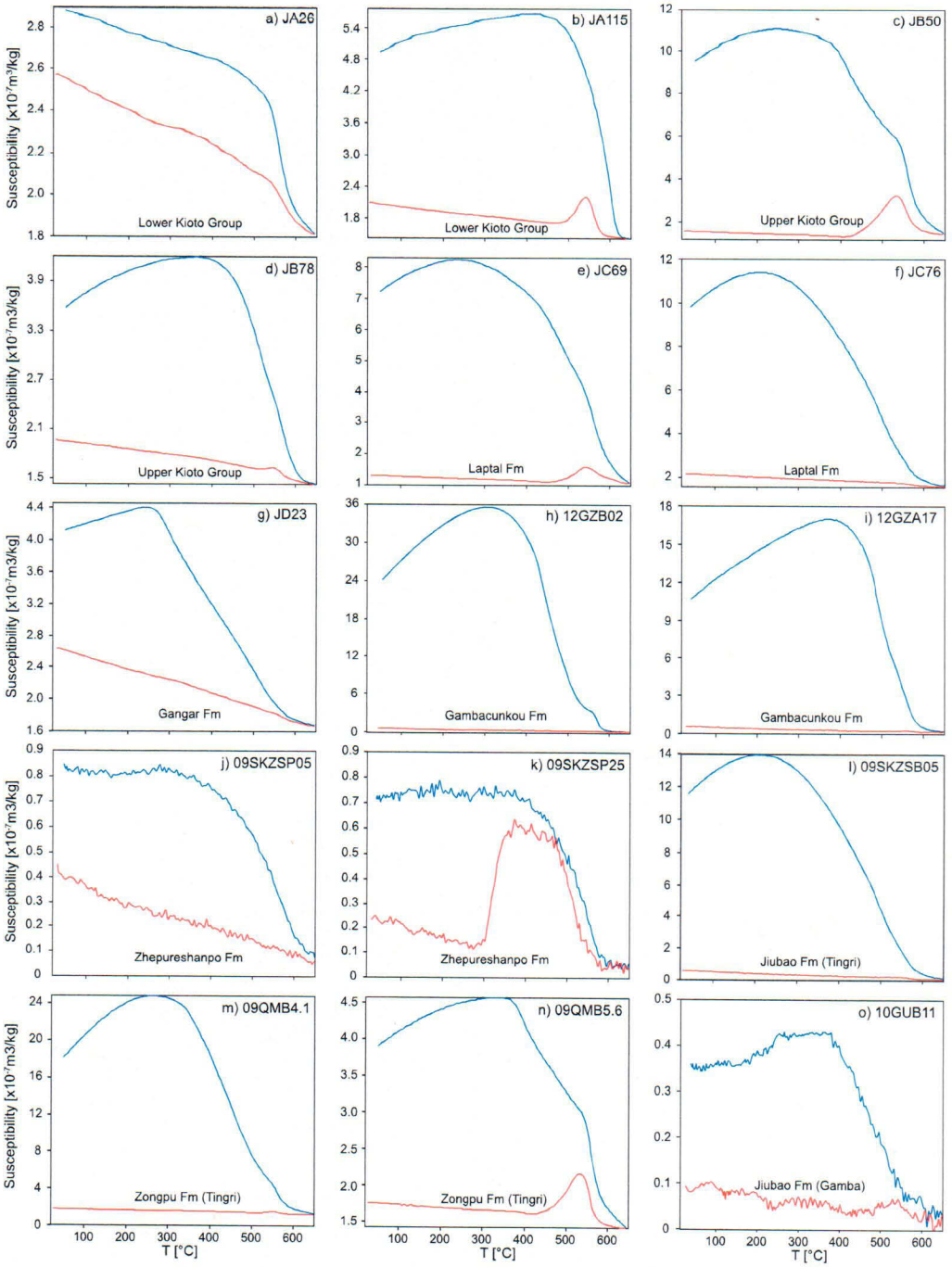

Figure 3. High-temperature heating (red) and cooling curves (blue) of bulk magnetic susceptibility in air for representative carbonate specimens from the Tingri area.

of the alteration of pyrite and possibly other Fe-bearing minerals [e.g., *Liu et al.*, 2005]. Also, detaching of Fe-bearing coatings on silicates can lead to magnetite formation during heating. High-temperature susceptibility experiments performed on the Wölong volcaniclastic sandstones yield results (Figures 5a–5d) similar to those of the carbonate specimens (Figures 3 and 4a–4d). All specimens show a rapid decrease in magnetization with increasing temperature up to 580°C, typical for magnetite. Some specimens are also characterized by an increase in susceptibility above 420°C (Figure 5d), consistent with the aforementioned

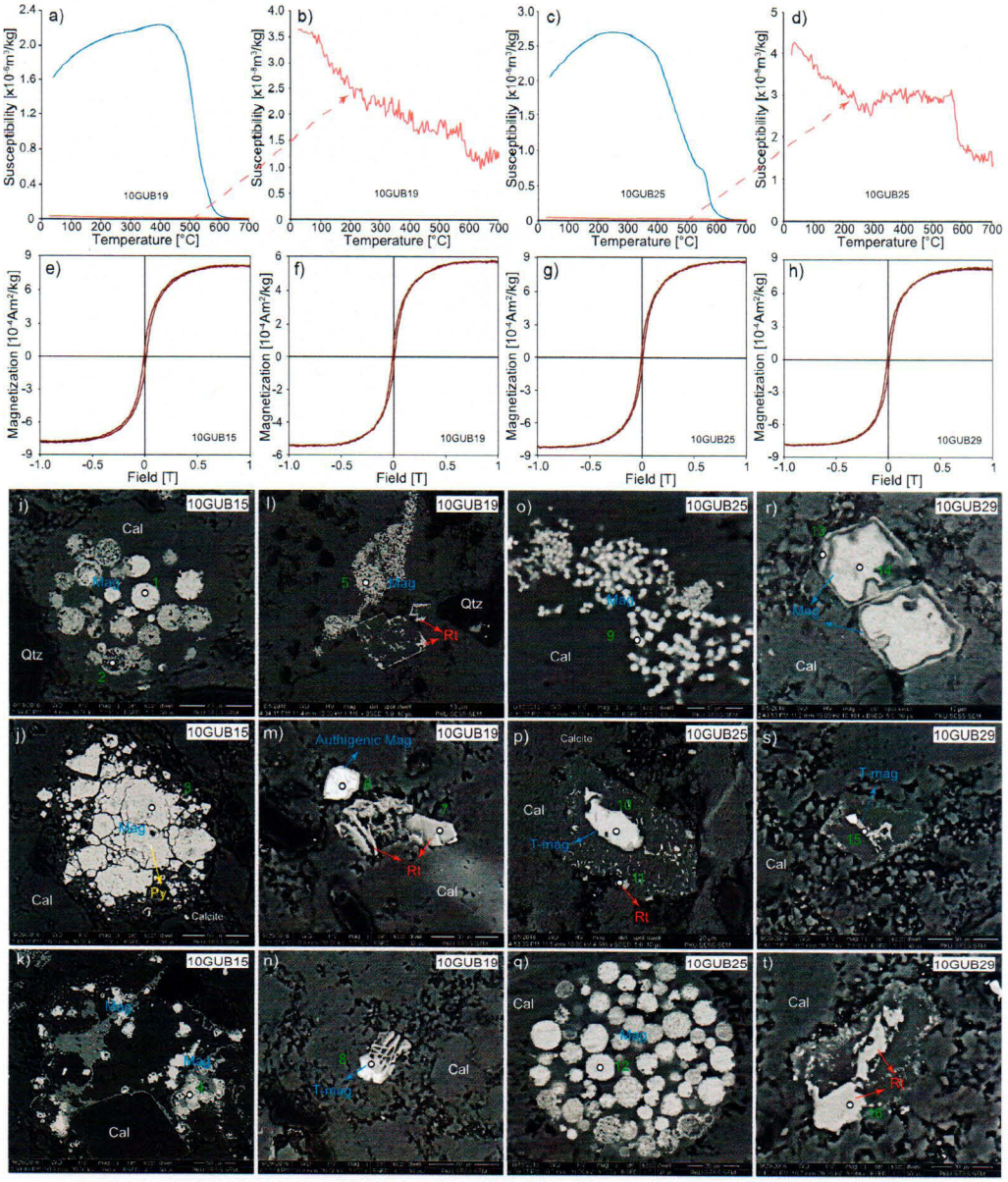

Figure 4. (a–d) High-temperature bulk susceptibility measurements for representative carbonate specimens from the Zongshan Formation in the Gamba area; Figures 4b and 4d are the enlarged heating curves of curves shown in Figures 4a and 4c, respectively. (e–h) Room temperature hysteresis loops from carbonate specimens of the Zongshan Formation. (i–t) SEM backscattered electron images for specimens of the Zongshan carbonate rocks. Mag: magnetite, Cal: calcite, Qtz: quartz, Py: pyrite, Rt: rutile, and Sp: sphalerite. White dots with numbers indicate the spots of the EDS analysis shown in Figure S2 and Table S5 in the supporting information.

oxidation of pyrite. Additional loss of susceptibility in most specimens up to 650°C (Figures 5a–5d) indicates that hematite makes a minor contribution to the bulk susceptibility.

3.2. Room Temperature Hysteresis Measurements

Hysteresis loops for each of the carbonate specimens, except those from the Zongshan Formation (Figures 4e–4h), are "wasp waisted" (Figures 6a–6r), indicating the combination of two or more magnetic components with contrasting coercivities [*Jackson*, 1990; *Roberts et al.*, 1995] or different size fractions of a single mineral [*Tauxe et al.*, 1996; *Dunlop*, 2002]. The low B_c and B_{cr} values for most specimens indicate

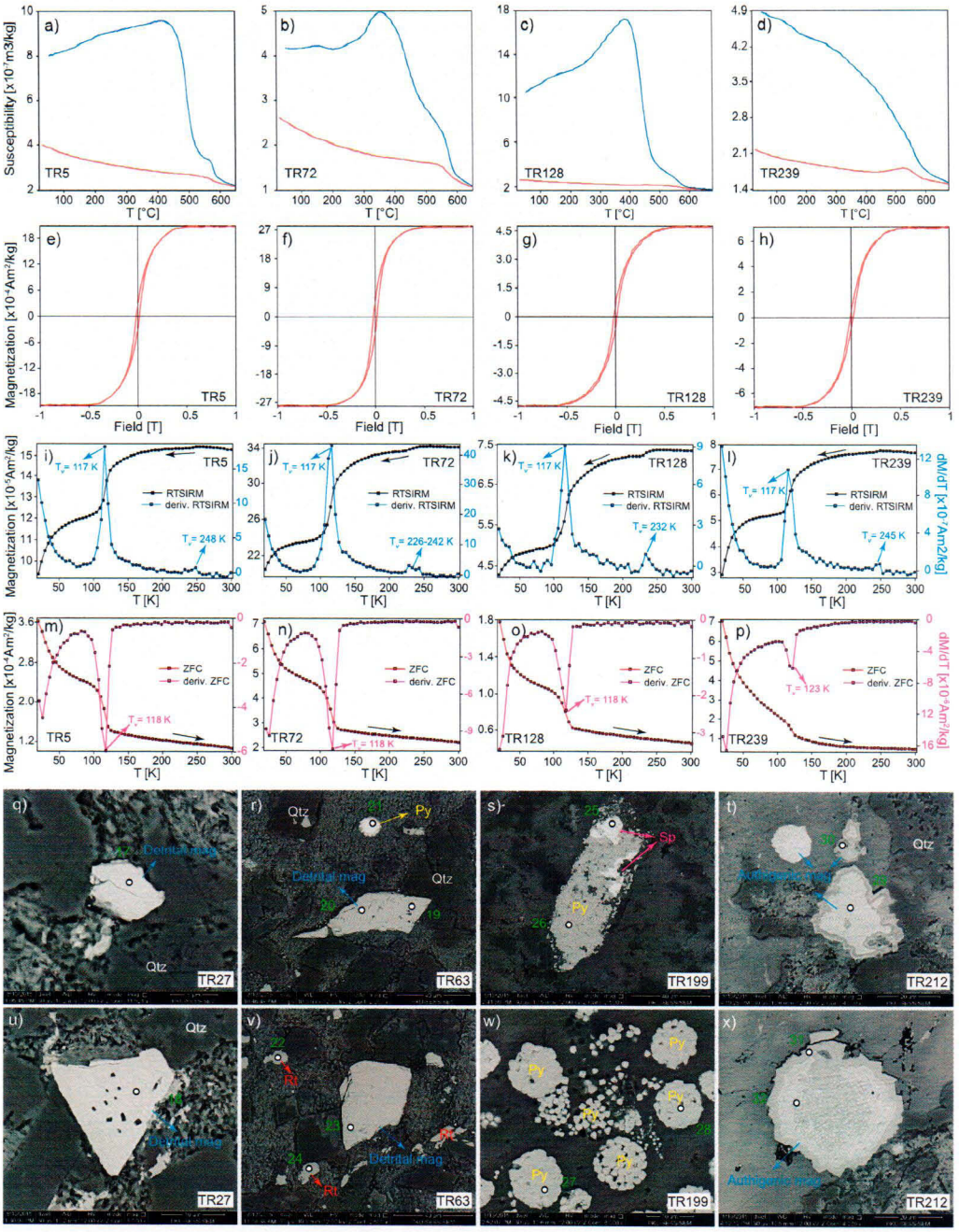

Figure 5. (a–d) High-temperature bulk susceptibility measurements for representative volcaniclastic specimens from the Wölong Formation. (e–h) Room temperature hysteresis loops for corresponding volcaniclastic specimens in Figures 5a–5d. (i–l) Low-temperature cooling of room temperature SIRM data and associated derivative for the specimens shown in Figures 5a–5d. (m–p) Thermal demagnetization of low-temperature SIRM data and their derivative after ZFC treatment for the specimens shown in Figures 5a–5d. (q–x) SEM backscattered electron images for volcaniclastic specimens from the Wölong Formation. Symbols are the same as those in Figures 4i–4t. TR27, TR63, and TR 199 are fresh specimens, whereas TR212 is a weathered specimen.

that the dominant magnetic carrier has a low coercivity (Table S2 in the supporting information). Most specimens are essentially saturated at 500 mT (Figure 6); others show a slow approach to saturation and an irreversible magnetization in the field range of 0.5–1 T (Figure 6), indicating a minor contribution from magnetic mineral(s) with higher coercivities. These observations indicate that magnetite with

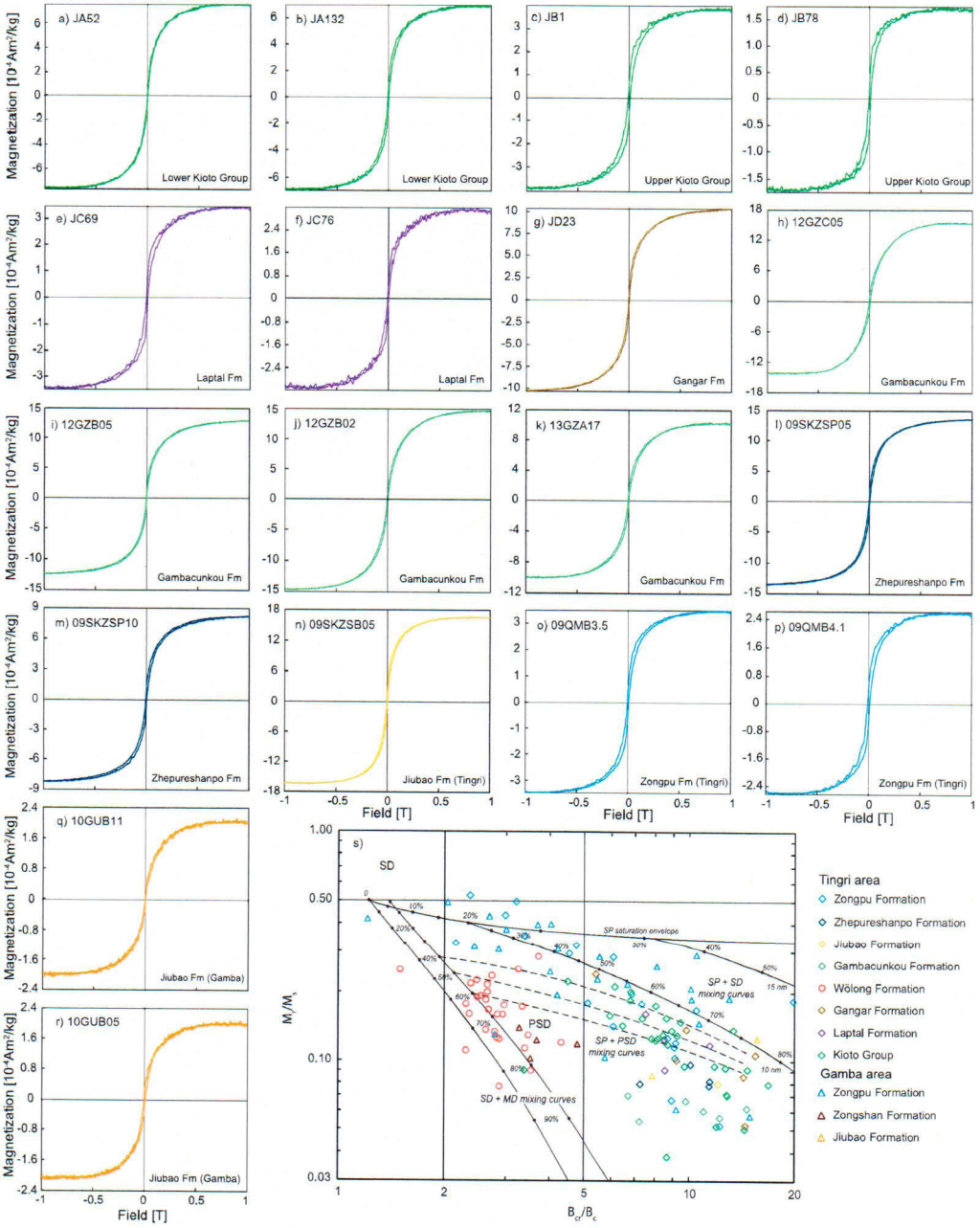

Figure 6. (a–r) Room temperature magnetic hysteresis loops from representative carbonate specimens from the Jurassic-Paleogene strata in the Tingri area and Jiubao Formation in the Gamba area. All the loops are wasp waisted. (s) Day plot [*Dunlop*, 2002] of the hysteresis parameters for carbonate and volcaniclastic specimens from the Tingri and Gamba areas. Part of the hysteresis data of the Kioto Group, Laptal, Gangar, and Wölong Formations are from *Huang et al.* [2015c]. The hysteresis data of the Zongpu Formation in the Gamba area are from *Huang et al.* [2017].

contrasting size fractions is the dominant magnetic carrier for these carbonate rocks, whereas the contribution to magnetization from hematite is minor. This is consistent with the results from the thermomagnetic experiments.

In contrast to the wasp-waisted shape of the hysteresis loops for carbonate specimens from the Jurassic to Paleogene strata in the Tingri area and Jiubao and Zongpu Formations in the Gamba area [*Huang et al.*, 2015c, 2017] (Figure 6), hysteresis loops for the carbonate specimens from the Zongshan Formation and

volcaniclastic specimens from the Wölong Formation are "pot bellied" (Figures 4 and 5). Compared to carbonate rocks with wasp-waisted loops, these specimens with pot-bellied loops have relatively higher B_c and lower B_{cr} values (Table S2). Together with the saturation by 0.5 T (Figures 4e–4h and 5e–5h), hysteresis characteristics indicate the dominance of a low-coercivity component, probably magnetite, in these specimens.

On a Day plot (Figure 6s), hysteresis data of carbonate specimens from the Jurassic to Paleogene strata in the Tingri area and Jiubao Formation in the Gamba area plot near the superparamagnetic (SP) + single domain (SD) mixing curves or SP + pseudosingle domain (PSD) mixing curves [*Day et al.*, 1977; *Dunlop*, 2002]. When hysteresis data of the Zongpu carbonate rocks in the Gamba area are also plotted [*Huang et al.*, 2017], there is a trend that most Paleogene specimens are distributed along the SP + SD mixing curves, whereas Mesozoic specimens cluster in the SP + PSD region (Figure 6s). The low B_c and B_{cr} values indicate that the wasp-waisted loops for these specimens cannot be attributed to hard antiferromagnetic admixtures (Table S2). Instead, they are likely the result of the combination of SD/PSD and SP magnetite in the specimens. In contrast, most specimens from the Zongshan and Wölong Formations plot near the SD + multidomain (MD) mixing curves (Figure 6s).

3.3. Low-Temperature Magnetic Properties

3.3.1. Low-Temperature Hysteresis Loops

Low-temperature hysteresis measurements on a representative carbonate specimen JB66 from the upper Kioto Group (Tingri area) show large and progressive increases in M_s, M_r, and B_c with a decrease in the temperature of the measurements (Figures 7a–7c). A broadening shift of the M_{rh} curves [*Rivas et al.*, 1981; *Fabian and Dobeneck*, 1997] indicates that the hysteresis loops become more open with decreasing temperature (Figure 7d). The shape of the loops transforms from wasp waisted to pot bellied (Figures 7b and 7c) as the SP fraction becomes thermally stable single domain (SSD) with cooling. At 40 K, M_s increases to 1.84 times its room temperature value, M_r increases to 2.25 times its room temperature value, and B_c changes to 2.09 times its room temperature value (Figures 7e–7g and Table S3 in the supporting information). These observations are consistent with a progressive translation of the SP-SSD threshold toward finer particle sizes upon cooling through. The sharp increase in M_s and M_r values below 40 K is partially due to the nonlinear paramagnetic signal affecting the approach-to-saturation calculations [*Jackson and Swanson-Hysell*, 2012]. It may also be caused by ordering of an unidentified iron-bearing phase [*Jackson and Worm*, 2001]. The shape parameter σ defined by *Fabian* [2003] quantifies the gradual shape change of the loops from strongly wasp waisted ($\sigma > 0$) to more pot bellied ($\sigma < 0$) at low temperature (Figure 7h). The transition between positive and negative σ values occurs below 30 K for specimen JB66 (Table S3).

3.3.2. Low-Temperature Room Temperature Saturation Isothermal Remanent Magnetization Cooling and Saturation Isothermal Remanent Magnetization Warming

Low-temperature cooling (LTC) curves of a Room Temperature Saturation Isothermal Remanent Magnetization (RTSIRM) in each of the carbonate specimens first increase in remanence during cooling (Figures 8a–8h). Most carbonate specimens then show a small decrease in magnetization at approximately 225 K (Figures 8c–8g), which is associated with the Morin transition and therefore the minor presence of nanoparticle hematite [*Özdemir et al.*, 2008]. After the small decrease, the remanence of most specimens continues increasing and arrives a broad maximum around 150–200 K (Figures 8a and 8c–8f) or 120–170 K (Figures 8g and 8h). No sharp change in magnetic properties is observed between 110 and 120 K (the Verwey transition, T_v in magnetite) (Figures 8a–8h) [*Özdemir et al.*, 1993], and we infer that the broad maximum and suppressed Verwey transition are likely to be associated with partial maghemitization of magnetite [*Özdemir et al.*, 1993; *Özdemir and Dunlop*, 2010]. Specimen JA132 has a monotonic increase in remanence down to 50 K (Figure 8b), indicating that magnetite has been essentially completely maghemitized [*Özdemir et al.*, 1993; *Özdemir and Dunlop*, 2010; *Chang et al.*, 2013].

The low-temperature zero-field cooled (ZFC) SIRM warming curves for all carbonate specimens undergo a monotonic decrease without a Verwey transition (Figures 8i–8p). Between 20 and 40 K, the low-temperature ZFC SIRM exhibits a sharp decrease of ~40% for specimens from the Jurassic strata and ~30% for specimens from the Paleogene strata (Figures 8i–8p). Similar sharp drops have been interpreted as evidence for nanoscale magnetic particles with an oxidized surface shell and unoxidized magnetite core [*Özdemir et al.*, 1993]. The oxidized surface shell with a smaller lattice parameter than the unoxidized magnetite core will stretch and ultimately crack, which can significantly reduce the volume of stoichiometric magnetite and lead to

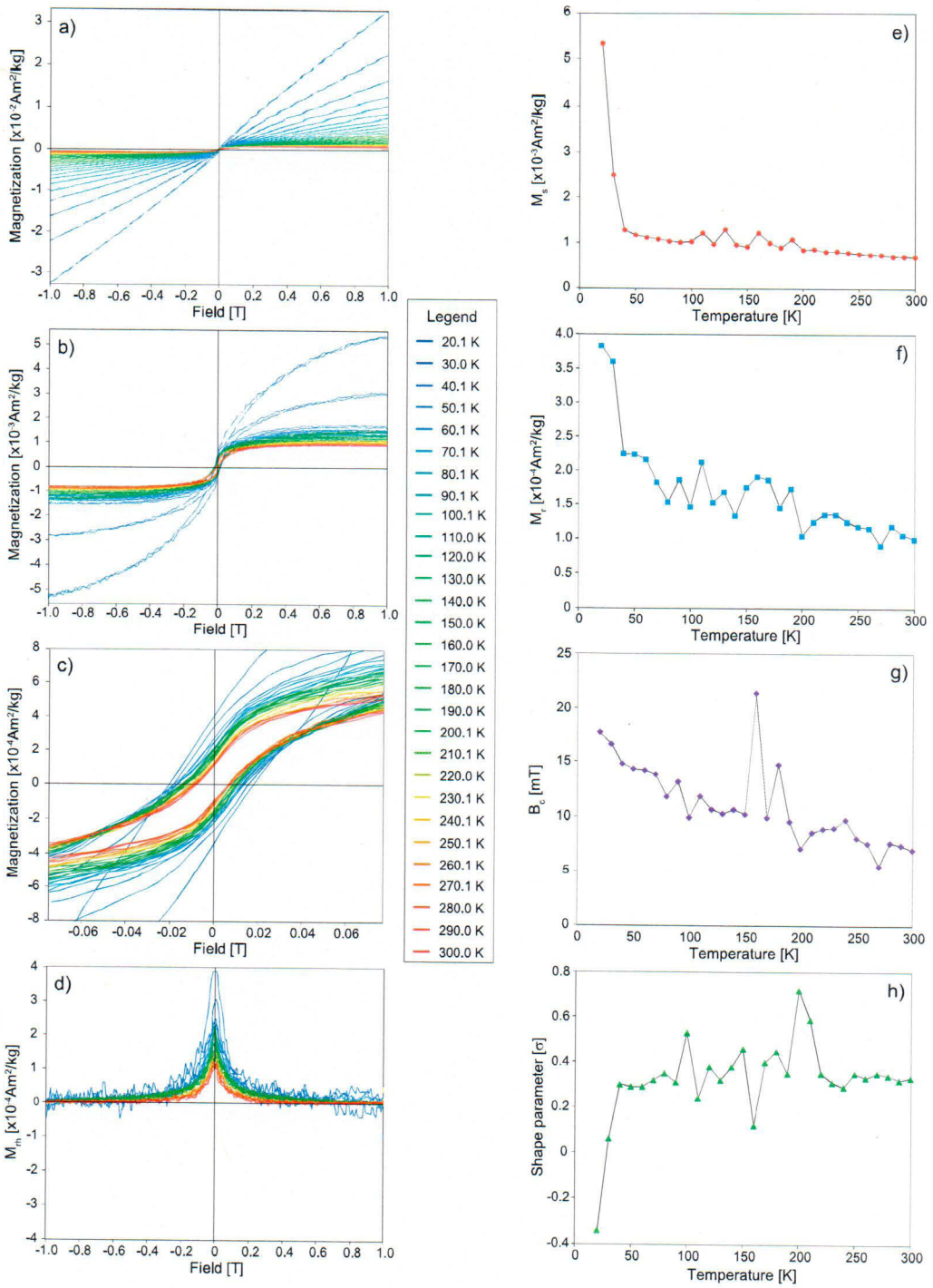

Figure 7. (a–c) Low-temperature magnetic hysteresis loops for carbonate specimen JB66 from the Upper Kioto Group. Figure 7a shows before correction for paramagnetic contribution. Figure 7b shows after correction for paramagnetic contribution. Figures 7c shows expanded view of the low-field portion of the loops in Figure 7b. The shape of the loops gradually changes from wasp waisted to pot bellied as temperature decreases to 20 K. (d) M_{rh} curves as a function of decreasing temperature for JB66. (e) Saturation magnetization, (f) saturation remanent magnetization, (g) coercive force, and (h) shape parameter [*Fabian*, 2003] of JB66 after correction for paramagnetic contribution, all as a function of temperature. Hysteresis data are presented in Table S3.

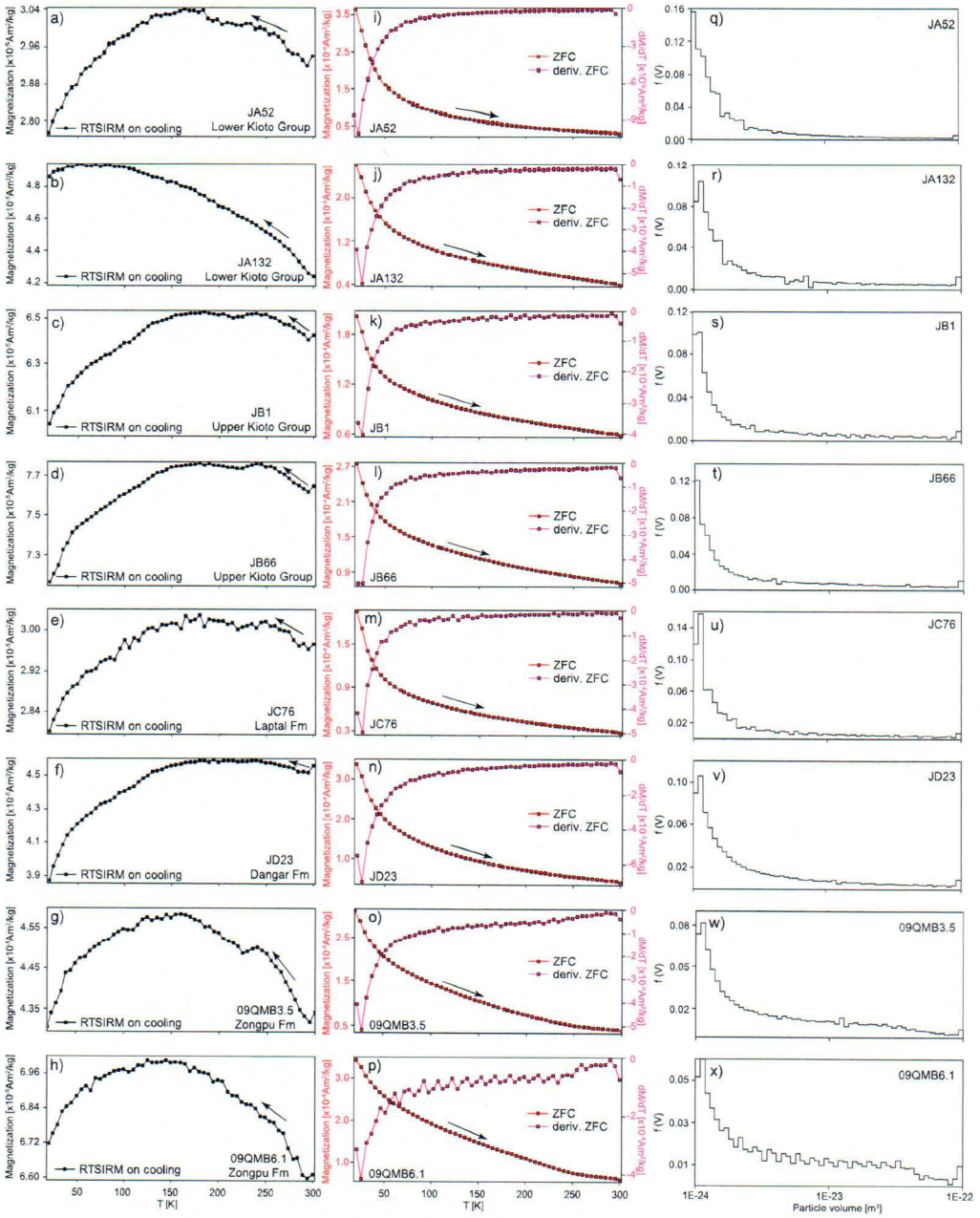

Figure 8. (a–h) Low-temperature cooling curves of RTSIRM for representative carbonate specimens from the Kioto Group and the Laptal, Dangar, and Zongpu Formations in the Tingri area. (i–p) Thermal demagnetization of low-temperature SIRM after ZFC treatment and their derivative data for specimens in Figures 8a–8h show progressive unblocking of the nano-phase ferrimagnets with increasing temperature. (q–x) Particle size distribution calculated from the ZFC SIRM curves in Figures 8i–8p following the procedure described by *Worm and Jackson* [1999].

strong superparamagnetism [*Özdemir et al.*, 1993]. ZFC SIRM curves also show that the total decrease in remanence is 82–93% for specimens from the lower Kioto Group, and Laptal and Dangar Formations (Tingri area), 70–79% for specimens from the upper Kioto Group, and 64–92% for specimens from the Zongpu Formation (Tingri area) (Figures 8i–8p), indicating significant concentrations of SP particles that undergo unblocking at low temperatures during ZFC SIRM warming. These observations further imply that specimens from the lower Kioto Group, Laptal, and Dangar Formations have a relatively larger fraction of fine-grained SP magnetite at room temperature than specimens from the upper Kioto Group and the

Zongpu Formation. Calculation of the particle size distribution from ZFC SIRM curves using the method of *Worm and Jackson* [1999] indicates a broad, unimodal size distribution of the SP particles with peaks at ~10^{-24} m^3 (10 nm in diameter) (Figures 8q–8x). Careful inspection of the calculated particle size distribution also indicates that the fraction of magnetite with a volume $\leq 3.2 \times 10^{-24}$ m^3 (~15 nm in diameter) in specimens from the Jurassic strata is larger than that in specimens from the Paleogene Zongpu Formation (Figures 8q–8x). These results are in good agreement with most of the room temperature hysteresis data, which plot along the SP-SD or SP-PSD mixing curves in the Day plot (Figure 6s) [*Dunlop*, 2002].

In the LTC RTSIRM curves of volcaniclastic specimens from the Wölong Formation (Tingri area), the remanence first increases slightly then shows a small drop at 226–248 K and an extremely sharp drop at 117 K during cooling, as indicated by the derivative of the LTC curves (Figures 5i–5l). These observations are consistent with the Morin transition for hematite [*Özdemir et al.*, 2008] and Verwey transition for inorganic magnetite [*Özdemir et al.*, 1993]. ZFC SIRM warming curves for specimens TR5, TR72, and TR128 show distinct warming features across the Verwey transition with the T_v calculated from the derivative of remanence versus temperature at 118 K (Figures 5m–5o). The Verwey transition for specimen TR239 is weak and has a calculated T_v of 123 K (Figure 5p).

3.3.3. Low-Temperature AC Susceptibility

In general, the measured susceptibilities of these specimens depend strongly on frequency and temperature (Figure 9). The in-phase susceptibilities (χ') and the out-of-phase susceptibilities (χ'') generally decrease and increase in magnitude with increasing frequency, respectively, indicating a broad distribution of nanoscale magnetite. χ'' remains much smaller than χ' for all frequencies and temperatures. The χ' of specimen JA52 exhibits maxima that decrease in magnitude and shift toward higher temperatures with increasing frequencies (Figure 9a). The χ'' component of JA52 also exhibits maxima occurring at lower temperatures than those of χ' (Figures 9a and 9b). For specimens JB66, JD23, and 09QMB6.1, the χ' at multiple frequencies decreases significantly when warming from 20 K to 50 K (Figures 9c, 9e, and 9g). We attribute this mainly to the presence of paramagnetic materials, where paramagnetic susceptibility depends inversely on absolute temperature and has no frequency dependence. In contrast to the very strong frequency dependence of χ' for specimen JA52 down to 20 K, the frequency dependence of χ' for specimens JB66, 09QMB6.1, and especially for JD23 is relatively weak at 20 K (Figures 9c, 9e, and 9g). However, χ' of these specimens diverges quickly at different frequencies as temperature increases, indicating that the SP-SSD threshold shifts to larger sizes and some SSD particles become gradually unblocked and exhibit SP behavior with increasing temperature. The sharp increase and very strong frequency dependence of χ' at 20–40 K probably indicate that the fraction of very fine grained (~10 nm) magnetite in specimen JA52 is significant [*Worm and Jackson*, 1999], which is consistent with the calculated particle size distribution from ZFC SIRM warming curves (Figure 8q). Although the measured χ'' is noisy (especially at high frequencies, as is typical for MPMS instruments), it is generally indistinguishable from the calculated values of $-(\pi/2)\, d\chi'/d(\ln(f))$ (Figures 9b, 9d, 9f, and 9h), where f is the frequency, defined by the Néel relation [*Néel*, 1949], implying that χ'' originates primarily in a thermal relaxation mechanism.

4. SEM Observation and EDS Analysis

To supplement our recent petrographic work on the Jurassic carbonate (10 specimens) and Lower Cretaceous volcaniclastic strata (seven specimens) in Section I [*Huang et al.*, 2015c] (see also supporting information Text S1), here we made SEM observations with EDS analysis on 38 carbonate and volcaniclastic specimens from the Cretaceous and Paleogene strata (six from Wölong in Tingri, seven from Gambacunkou in Tingri, one from Jiubao in Tingri, six from Zhepureshanpo in Tingri, 11 from Zongpu in Tingri, three from Jiubao in Gamba, and four from Zongshan in Gamba). SEM observations were conducted on a FEI GEG-650 scanning electron microscope, operated at 12 or 15 kV and 40–60 nA at the SEM laboratory at the Key Laboratory of Orogenic Belts and Crustal Evolution, School of Earth and Space Sciences, Peking University (Beijing, China). EDS analysis was subsequently conducted to obtain compositional information.

Similar to what we observed in the Jurassic carbonate rocks in Section I [*Huang et al.*, 2015c], two different morphologies of magnetic minerals are identified in the Late Cretaceous to early Paleogene carbonate rocks excluding those from the Zongshan Formation in the Gamba area (Figure 10). We interpret both of these populations to be composed of magnetite based on the EDS analysis (Figure S1 and Table S4 in the

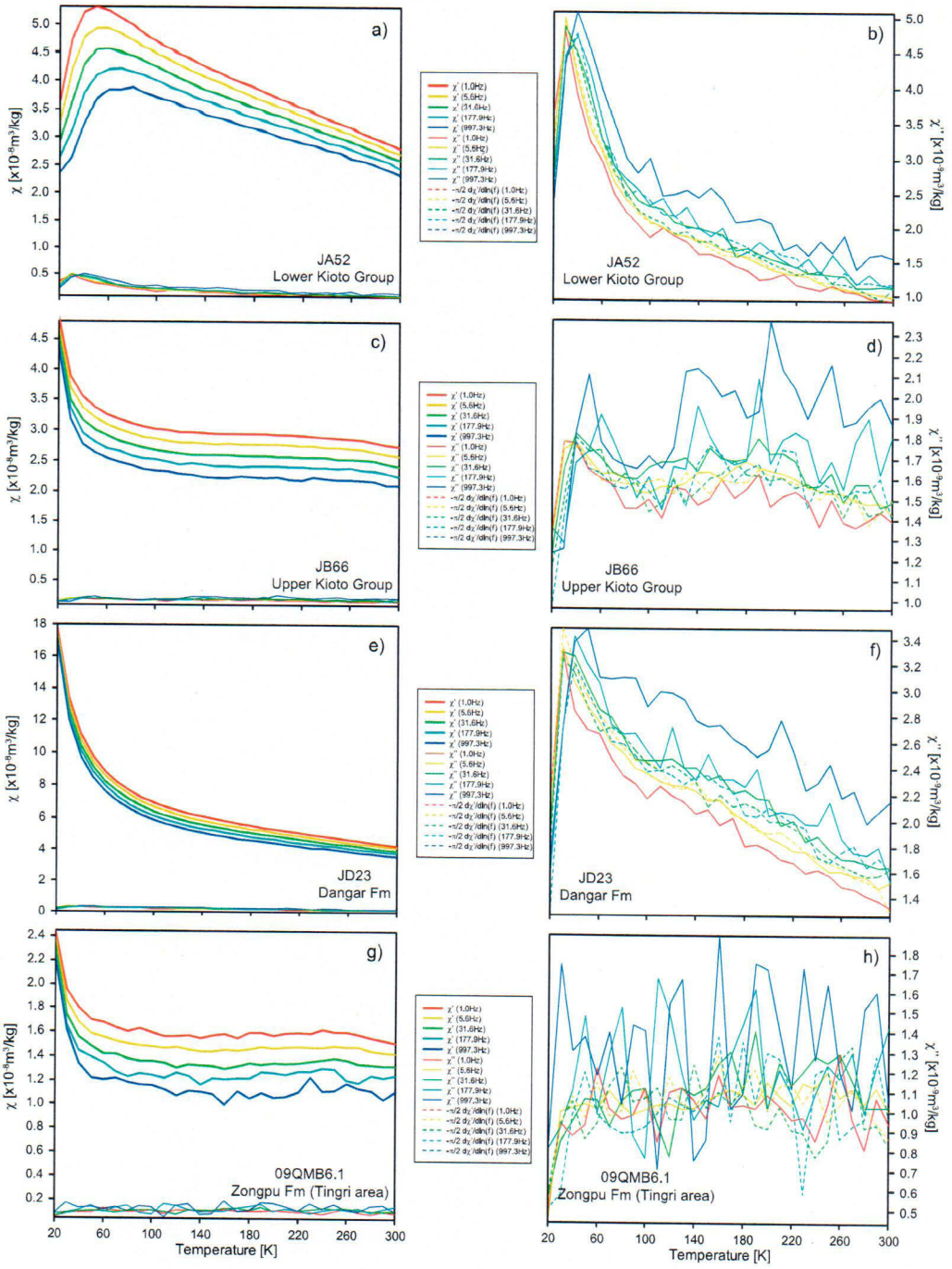

Figure 9. (a, c, e, and g) In-phase and quadrature susceptibility at 1.0 Hz, 5.6 Hz, 31.6 Hz, 177.9 Hz, and 997.3 Hz for carbonate specimens JA52, JB66, JD23, and 09QMB6.1 from the Tingri area, measured from 20 to 300 K. (b, d, f, and h) Expanded view of quadrature susceptibilities, compared to the derivative of in-phase susceptibility with respect to ln(*f*).

supporting information) and rock magnetic results. One group comprises framboid aggregating up to 80 μm in diameter (Figures 10b–10e, 10g–10i, 10o, 10s, and 10v–10x). The framboids are typically either loosely or tightly clustered subeuhedral to euhedral magnetite crystals of up a few micrometers in size. Some finer particles can be seen, but the population with a particle diameter of ~10 nm inferred from LT measurements could not be resolved with the SEM. Some of the euhedral magnetite crystals within the

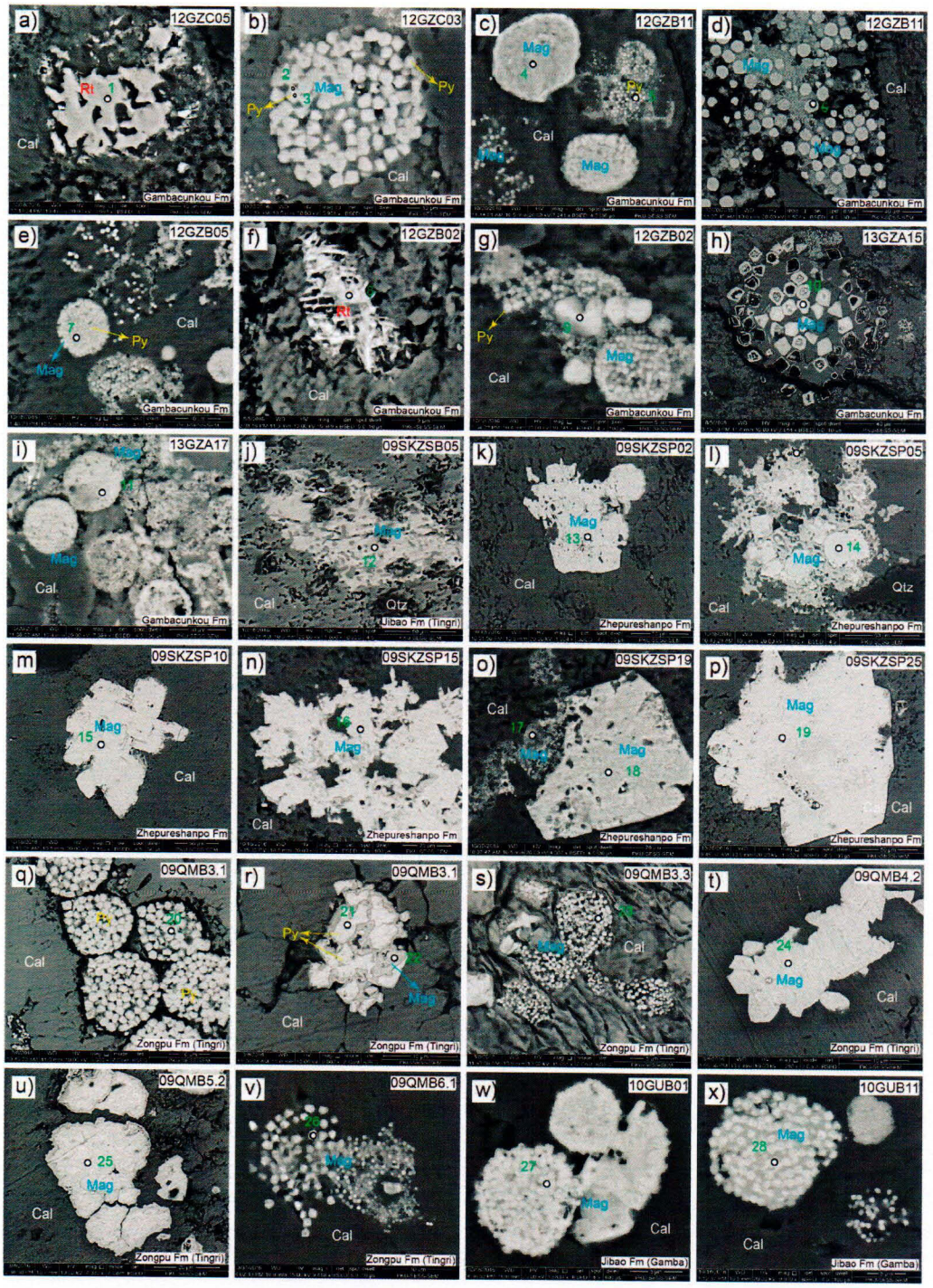

Figure 10. SEM backscattered electron images for representative carbonate specimens of the upper Cretaceous to Paleogene strata in the Tingri area and the Jiubao Formation in the Gamba area. Symbols are the same as those in Figures 4i–4t. Results of EDS analysis are shown in Figure S1 and Table S4. SEM backscattered electron images for carbonate specimens of the Kioto Group and the Laptal and Dangar Formations are presented in *Huang et al.* [2015c].

framboids show growth zoning (Figure 10h). The second phase of magnetite is subeuhedral to euhedral with crystal sizes ranging from a few micrometers to >100 μm (Figures 10j–10p, 10r, 10t, and 10u). Rims with darker backscattered electron images are usually observed around these subeuhedral to euhedral

magnetite crystals (Figures 10l, 10n, and 10u). We also observe iron sulfides with brighter backscattered electron images (Figures 10b, 10c, 10e, 10g, and 10r). These grains usually occur as framboids (Figure 10q), may be present in the cores of fine-grained magnetite crystals in the framboids (Figures 10b, 10c, 10e, and 10g), or are the cores of subeuhedral to euhedral magnetite crystals (Figure 10r). Rutile (Figure 10a) is usually pseudomorphic after titanomagnetite and exists as rims of or as inclusion in the preexisting titanomagnetite. Rutile can also be a solid-state exsolution feature of titanomagnetite, as when they occur as trellises composed of rutile lamellae (Figure 9f). The rutile is thus the diagenetic alteration product of detrital titanomagnetite with iron completely leached from the particles. Thus, we observe no detrital magnetite, but our petrography shows abundant authigenic magnetite that likely formed as an oxidation product of pyrite or other iron sulfides.

In the carbonate specimens from the Zongshan Formation in the Gamba area, we identified magnetite with both framboidal (Figures 4i, 4l, 4o, and 4q) and subeuhedral to euhedral (Figures 4j, 4k, and 4r) morphologies (Figure S2 and Table S5 in the supporting information). These magnetite grains have a clear authigenic origin with characteristics similar to those described in the precede paragraph. The rutile is pseudomorphic after titanomagnetite (Figures 4l, 4p, 4s, 4t, and S2), just as we found in other carbonate rocks (Figures 10a and 10f). Moreover, a minor phase of detrital titanomagnetite was identified (Figures 4n, 4p, and 4s). These titanomagnetite grains survived the diagenetic alteration with iron partially to completely preserved (Figure S2 and Table S5).

In the volcaniclastic specimens from the Wölong Formation, we identified detrital magnetite (Figures 5q, 5r, 5u, 5v, and S2 and Table S5) from dark blue fresh specimens with a well-defined characteristic remanent magnetization (ChRM, Figures S3e–S3g in the supporting information). Framboidal and subeuhedral to euhedral authigenic magnetite was also observed in some yellowish weathered specimens (Figures 5t and 5x), from which a recent overprint by the present-day geomagnetic field (PDF) was isolated (Figure S3h). Some detrital titanomagnetite grains have been completely altered to amorphous rutile with little iron left in the crystal (Figures 5v and S2 and Table S3). Pyrite and sphalerite are not oxidized in these fresh specimens (Figures 5r, 5s, and 5w), but pyrite is oxidized to magnetite in the weathered specimens (Figures 5t and 5x). These observations are consistent with our previous SEM and EDS work on the Wölong volcaniclastic rocks [*Huang et al.*, 2015c].

5. Discussion

5.1. Origin of ChRM Retained in the Zongshan Carbonate Rocks and Wölong Volcaniclastic Sandstones

Carbonate rocks from the Zongshan Formation in the Gamba area have been used to constrain the latest Cretaceous paleolatitude (pole 22 in Figure 1c and Table S1) of the Tibetan Himalaya and therefore the dimensions of Greater India [*Patzelt et al.*, 1996]. Our recent work has shown that fold tests of the ChRMs from these rocks are inconclusive and that these carbonate rocks are almost certainly remagnetized [*Huang et al.*, 2017]. Here we provide detailed rock magnetic and petrographic work to substantiate that argument. Our thermomagnetic experiments and hysteresis measurements indicate that magnetite is the dominant magnetic carrier in these rocks, consistent with previous rock magnetic work [*Patzelt et al.*, 1996]. Our SEM observations and EDS analysis, however, show that detrital (titano)magnetite has been extensively altered to rutile with few (titano)magnetite grains preserved (Figures 4l–4n, 4p, 4s, and 4t). In contrast, authigenic magnetite pseudomorphic after framboidal or subeuhedral to euhedral pyrite is omnipresent in these rocks (Figures 4i–4l, 4o, 4q, and 4r). Therefore, the CRM carried by authigenic magnetite with a broad size distribution is strong enough to "swamp" the primary depositional remanent magnetite (DRM) carried by detrital (titano)magnetite. We argue that the ChRM isolated by either alternating field (AF) or thermal demagnetization is probably a combination of CRM and minor DRM and therefore cannot faithfully represent the primary NRM induced by the geomagnetic field during the deposition of these rocks. Thus, the latitude of the Tibetan Himalaya during latest Cretaceous times determined from the Zongshan carbonate rocks so far published is unreliable.

The ChRM isolated from the volcaniclastic sandstones of the Wölong Formation has been interpreted to be primary and used to determine the Early Cretaceous latitude of the Tibetan Himalaya. The applied elongation/inclination correction [*Tauxe and Kent*, 2004] suggests that inclination shallowing, as often observed in clastic rocks [*Kodama*, 2009; *Huang et al.*, 2013], is negligible [*Huang et al.*, 2015c]. The

calculated paleolatitude (pole 24 in Figure 1c and Table S1) is consistent with results reported from coeval volcaniclastic sandstones (pole 23 in Figure 1c) and lavas (poles 25 and 26) in southern Tibet [*Klootwijk and Bingham*, 1980; *Yang et al.*, 2015; *Ma et al.*, 2016]. Our new extensive rock magnetic and petrographic investigation further supports the interpretation that the NRM is primary. For these dark blue, fresh volcaniclastic sandstone specimens, thermomagnetic experiments, hysteresis measurements, and low-temperature remanence tests consistently indicate that the dominant magnetic carrier is pseudosingle domain (PSD) magnetite with a T_v of 117 K and that the contribution from hematite is limited (Figures 5 and 6s) [*Huang et al.*, 2015c]. SEM observations further indicate that detrital magnetite is widespread and that authigenic magnetite formed during pyrite oxidation appears to be absent (Figures 5q–5s and 5u–5w). Therefore, the fresh volcaniclastic sandstones of the Wölong Formation retain a primary depositional remanent magnetite (DRM) carried by magnetite. For the yellowish weathered volcaniclastic specimens, an overprint by PDF is usually isolated below 20 mT or 200°C and no stable ChRM can be determined (Figure S3 in the supporting information) [*Huang et al.*, 2015c]. Thermomagnetic experiments, hysteresis measurements performed in this work, and end-member modeling of IRM [*Huang et al.*, 2015c] show the presence of hematite in these specimens, which is also indicated by the small drop in remanence during the Morin transition in the LTC RTSIRM curves (Figure 5l). Detrital magnetite should still have a significant contribution to the remanence in these specimens as indicated by the distinctive drop in remanence across Verwey transition in the LTC RTSIRM curves (Figure 5l). The ZFC SIRM warming curves, however, show a blurred Verwey transition with a much smaller peak at higher temperatures (~123 K) (Figure 5p). It is very likely that the Verwey transition is smeared out by progressive unblocking of SP authigenic magnetite [*Moskowitz et al.*, 1989]; this is supported by the observation of authigenic magnetite formed as a product of pyrite oxidation (Figures 5t and 5x). A stable primary DRM was probably partially destroyed by alteration of the detrital magnetite or was contaminated by the CRM residing in SSD magnetite, which is cogenetic to the authigenic SP fraction. Fortunately, most volcaniclastic specimens from the Wölong Formation are fresh or experienced only weak incipient weathering to retain a primary DRM, whereas strongly weathered specimens are found only near the top of Section I [*Huang et al.*, 2015c].

5.2. Mechanisms for Remagnetization of the Carbonate Rocks Across Himalaya

While thermoviscous resetting might be a plausible scenario to explain remagnetization of carbonate rocks under specific conditions [e.g., *Kent*, 1985], the prevailing mechanism involves chemical alteration and growth of authigenic magnetic minerals at temperatures below their Curie temperatures [e.g., *McCabe and Elmore*, 1989; *Dekkers*, 2012; *Jackson and Swanson-Hysell*, 2012; *van der Voo and Torsvik*, 2012]. Secondary NRMs residing in pyrrhotite have been commonly isolated from metamorphic rocks (mostly metacarbonate rocks) across the Himalaya [*Appel et al.*, 2012, and references therein]. The formation of pyrrhotite is largely due to desulphidation of pyrite under oxidizing conditions or breakdown of magnetite under reducing conditions at elevated temperature [e.g., *Ferry*, 1981; *Hall*, 1986; *Rochette*, 1987]. Pyrrhotite can also be formed extremely slowly at low temperature (<100°C) [e.g., *Larrasoaña et al.*, 2007; *Aubourg et al.*, 2012; *Roberts et al.*, 2013]. A primary NRM can be easily erased and replaced by secondary magnetization carried by pyrrhotite in metacarbonate rocks from the Himalaya. Our rock magnetic tests show, however, that pyrrhotite has no or little contribution to magnetic properties in the nonmetamorphosed carbonate rocks in the Tingri and Gamba areas.

Instead, we have identified that SP + SD and SP + PSD magnetite is the dominant magnetic carrier in these carbonate rocks. The SP fraction of magnetite is characterized by the low-temperature hysteresis, ZFC SIRM warming, and AC susceptibility measurements, which show strong temperature dependence of the hysteresis parameters (Figure 7), 64–93% remanence loss on warming from 20 to 300 K (Figures 8i–8p), and strong frequency dependence of in-phase susceptibility (Figure 9). The calculated particle size distribution of magnetite from ZFC SIRM curves indicates a broad, unimodal size distribution of the SP particles which peaks at a calculated ~10 nm grain diameter (Figures 8q–8x). Although the SP fraction of magnetite is not the carrier of the ancient NRM, it is crucial for understanding the origin of the (presumably) SD/PSD grain population: the SD/PSD grains are the large grain size end-members of the authigenic magnetite population [*Jackson and Swanson-Hysell*, 2012]. In these carbonate rocks, eolian delivery (including extraterrestrial fluxes) [e.g., *Oldfield et al.*, 1985; *Lanci and Kent*, 2006] or extracellular magnetite formation during microbial iron reduction [e.g., *Sparks et al.*, 1990; *Maloof et al.*, 2007] are probably not viable mechanisms for SP magnetite formation

because the characteristics of magnetite with these origins have not been identified in our rock magnetic tests and petrographic observations. Detrital magnetite grains in PSD/MD size range can also be transformed to SP-SD sizes by reductive dissolution during diagenesis [e.g., *Karlin and Levi*, 1983; *Smirnov and Tarduno*, 2001]. Given that major shortening accommodated by thrusting and folding occurred in the Himalaya after the onset of the India-Asia collision [*DeCelles et al.*, 2002; *Long et al.*, 2011] and marly limestones are common in the Jurassic to Paleogene strata of interest (Figure 2), pressure solution and transformation of iron-rich smectite to illite (containing less iron than smectite) + magnetite during clay diagenesis might be a source for formation of SP + SD/PSD magnetite [e.g., *Jackson et al.*, 1988; *McCabe and Elmore*, 1989; *Katz et al.*, 2000; *Zegers et al.*, 2003; *Tohver et al.*, 2008; *Zwing et al.*, 2009; *Elmore et al.*, 2012]. However, widespread authigenic magnetite pseudomorphic after pyrite, indicated by our SEM observations and EDS analyses (Figures 4 and 10), strongly suggests that oxidation of early diagenetic iron sulfides (i.e., pyrite or perhaps minor greigite) to magnetite is probably the principal mechanism for producing magnetite populations spanning the SP-SD/PSD range and inducing remagnetization of these carbonate rocks. This mechanism has also been widely documented in remagnetized carbonate rocks of the Appalachians in the U.S. [*Suk et al.*, 1990a, 1990b, 1993], the Cantabrian mountain chain in Spain [e.g., *Van der Voo et al.*, 1997; *Weil and Van der Voo*, 2002], and the carbonate rocks from the Zongpu Formation in the Gamba area [*Huang et al.*, 2017]. This process might be facilitated by the formation of a maghemite shell during subsequent oxidation of authigenic magnetite (see section 3.3.2), which can significantly reduce the grain size of the magnetite and may lead to strong superparamagnetism [*Özdemir et al.*, 1993].

Grain growth of authigenic magnetic particles is often assisted by fluid [e.g., *Dekkers*, 2012; *Elmore et al.*, 2012]. An origin from fluid circulation is strongly supported by the widespread calcite veins in the Jurassic to Paleogene carbonate rocks in the Tingri and Gamba areas [*Jadoul et al.*, 1998; *Hu et al.*, 2012; *Li et al.*, 2015; *Han et al.*, 2016]. Orogenic fluids, pumped by tectonically induced overpressures, or gravity, have also been argued to cause remagnetization in a variety of rocks in the Lhasa terrane [*Huang et al.*, 2015a, 2015b]. The directions of the isolated secondary remanence in the Paleogene carbonate rocks of the Zongpu Formation in the Gamba areas would imply paleolatitude of ~19°N, that is, adjacent to the southern margin of the Lhasa terrane during the early Paleogene [*Hu et al.*, 2016a; *Huang et al.*, 2017]. This likely indicates that remagnetization may be related to orogenic fluid flow within the Tibetan Himalaya shortly after the onset of the India-Asia collision, recently estimated to be ~59–56 Ma based on stratigraphic and sedimentological arguments [e.g., *Wang et al.*, 2011; *Hu et al.*, 2012, 2015a, 2015b, 2016a, 2016b, 2017; *DeCelles et al.*, 2014; *Orme et al.*, 2014; *Ding et al.*, 2016]. Nonetheless, we argue that it is unlikely that orogenic fluids are responsible for remagnetization of the Jurassic carbonate rocks in Section I given that the secondary NRM was induced at 23.8°S when the Tibetan Himalaya was far away from Asia [*Huang et al.*, 2015c]. It is difficult to evaluate the source of the fluid-induced remagnetization of the Jurassic carbonate rocks. It is clear, however, that these oxidizing fluids did not circulate through the overlying Lower Cretaceous volcaniclastic sandstones, because the thick intercalated organic-rich black shales of the Wölong Formation [*Huang et al.*, 2015c] probably acted as an aquitard.

Other workers have recognized that remagnetization can be associated with the depositional environment of the host carbonate rocks [*Zwing et al.*, 2005; *Jackson and Swanson-Hysell*, 2012]. Carbonate rocks with primary NRMs are usually deep water pelagic limestones with substantial contributions from detrital or biogenetic SD/PSD/MD magnetite [*Channell and McCabe*, 1994; *Tarduno and Myers*, 1994; *Abrajevitch and Kodama*, 2009; *Chang et al.*, 2013; *Roberts et al.*, 2013], whereas remagnetized carbonate rocks are commonly deposited in shallow-water environment. Most Jurassic-Paleogene limestones exposed in the Tingri and Gamba areas are, indeed, shallow-water carbonates deposited on a continental shelf or on a carbonate ramp [*Jadoul et al.*, 1998; *Hu et al.*, 2012; *Li et al.*, 2015; *Han et al.*, 2016]. The Upper Cretaceous carbonate rocks from the Gambacunkou and Jiubao Formations, however, accumulated in a hemipelagic and/or pelagic environment [*Willems et al.*, 1996; *Hu et al.*, 2012; *Li et al.*, 2015]. Low clastic influx and high carbonate productivity can explain the low concentration of detrital magnetite in these rocks. Because of reductive dissolution and authigenic magnetic particle growth assisted by oxidizing fluids during burial and diagenesis, we argue that the carbonate rocks of the Tibetan Himalaya rarely retain a primary NRM and, as a rule of thumb, are pervasively remagnetized, unless demonstrated otherwise.

We have documented evidence for pervasive remagnetization of the Jurassic to Paleogene carbonate rocks in the TH. Paleomagnetic poles 16–22 and 27 (Figure 1c) determined from these rocks are therefore unreliable and should not be used for tectonic reconstructions. The dimension of Greater India in Jurassic and

through Late Cretaceous to Paleogene remains unsolved, and the initiation of India-Asia collision cannot yet be constrained precisely by paleomagnetism [*Huang et al.*, 2017]. We also note that the paleolatitudes (poles 28–33 in Figure 1c) of Triassic rocks within the TH [*Klootwijk and Bingham*, 1980; *Klootwijk et al.*, 1983; *Appel et al.*, 1991; *Schill et al.*, 2002; *Ran et al.*, 2012] come from carbonate rocks. Despite the fact that the paleolatitudes that were calculated from these rocks follow the paleolatitudinal evolution of Gondwana in the Triassic [e.g., *Li et al.*, 2016], we here tentatively suggest that the reliability of these poles in the absence of the rigorous rock magnetic and electron microscopic assessment as presented in this paper requires further testing.

5.3. Criteria for Diagnosing Remagnetization of Carbonate Rocks in Southern Tibet

Besides the widespread secondary remanence residing in pyrrhotite [e.g., *Crouzet et al.*, 2001; *Appel et al.*, 2012], we have detected pervasive remagnetization residing in authigenic magnetite in unmetamorphosed carbonate rocks of the TH. Paleogeographic reconstructions of the Tibetan Himalaya and India-Asia collision could be seriously flawed when remagnetization of carbonate rocks is not identified. Therefore, below we outline criteria—room temperature hysteresis measurements, low-temperature hysteresis, RTSIRM, LTSIRM, and AC susceptibility, and electron microscopy—that are independent from paleomagnetic directions but can aid in recognizing cryptic remagnetization in a more robust way.

Similar to remagnetized carbonate rocks in North America and Europe [e.g., *McCabe et al.*, 1983; *Jackson*, 1990; *Suk et al.*, 1991; *Dinarès-Turell and Garcia-Senz*, 2000; *Weil and Van der Voo*, 2002; *Gong et al.*, 2009], we find that the remagnetized unmetamorphosed carbonate rocks from the TH contain high concentrations of authigenic fine-grained (SP) magnetite. Room temperature hysteresis loops of these remagnetized carbonate rocks are often wasp waisted and hysteresis parameters plot near the SP + SD/PSD mixing curves on Day plot (Figure 6), which are distinct from the trend of nonremagnetized pelagic carbonate rocks [e.g., *Channell and McCabe*, 1994; *Jackson and Swanson-Hysell*, 2012; *Roberts et al.*, 2013] and Wölong volcaniclastic sandstones (Figure 6). We note, however, that a remagnetization test based on room temperature hysteresis behavior is only robust when authigenic phases represent an overwhelming majority of the magnetic mineralogy and detrital phases are not present in significant amounts [*Zwing et al.*, 2005]. A special case is from the Zongshan carbonate rocks: although hysteresis loops are mostly pot bellied (Figures 4e–4h) and the hysteresis parameters mainly plot along the SD + MD mixing curves in the region of nonremagnetized carbonate rocks (Figure 6s), SEM observations show that authigenic magnetite has a greater abundance than detrital magnetite (Figures 4i–4t). Therefore, we conclude that carbonate rocks of the Zongshan Formation are partially remagnetized and should not be used for paleogeographic reconstructions. The failure of using hysteresis data to fingerprint remagnetization of Zongshan carbonate rocks is probably caused by the amount of detrital magnetite within the rocks, which shifts the peak of the size distribution into the PSD-MD range [*Jackson and Swanson-Hysell*, 2012]. Hysteresis loops favor larger grain size because of the large volume of such grains.

Another potential tool for diagnosing remagnetization of unmetamorphosed carbonate rocks utilizes the low-temperature rock magnetic properties. Suppressed Verwey transitions in both LTC RTSIRM and ZFC SIRM curves of the remagnetized carbonate rocks (Figure 8) are distinct from the clear Verwey transitions in nonremagnetized pelagic carbonate rocks [e.g., *Channell and McCabe*, 1994; *Abrajevitch and Kodama*, 2009; *Chang et al.*, 2013] and volcaniclastic sandstones (Figures 5i–5k and 5m–5o). The suppressed Verwey transition indicates that the magnetic carrier in remagnetized carbonate rocks is nonstoichiometric magnetite. The cation deficiency of the authigenic magnetite is probably the result of oxidation of iron sulfide to magnetite and subsequent (partial) maghemitization of this authigenic magnetite [*Özdemir et al.*, 1993; *Jackson and Swanson-Hysell*, 2012]. Nonremagnetized pelagic carbonate rocks often have stoichiometric detrital magnetite or biogenic magnetite as their dominant magnetic carrier which leads to well resolved Verwey transitions [e.g., *Moskowitz et al.*, 1993; *Channell and McCabe*, 1994; *Chang et al.*, 2013]. We note that a suppressed Verwey transition is also observed in pelagic carbonate rocks with highly to fully oxidized biogenic magnetite [e.g., *Chang et al.*, 2013]. However, the SP fraction in such rocks is usually limited, which is distinctly different from what we observe in remagnetized carbonate rocks, as evident in the shift of low-temperature hysteresis parameters (Figure 7), the remanence drop during ZFC SIRM warming (Figure 8), and temperature-dependent AC susceptibility (Figure 9). The carbonate rocks from the Zongshan Formation are a special case with both authigenic magnetite formed during oxidation of diagenetic pyrite and detrital magnetite.

Although no low-temperature rock magnetic data are available for these specimens, we predict a detectable Verwey transition in the LTC RTSIRM curves but a blurred or suppressed Verwey transition in the ZFC SIRM warming curves. The weathered volcaniclastic sandstones from the Wölong Formation (Figures 5l and 5p) show similar features, and the much lower concentration of detrital magnetite in carbonate rocks will make it more difficult for the Verwey transition to become visible, especially in ZFC SIRM warming curves. Therefore, low-temperature rock magnetic properties could possibly provide a more reliable tool than room temperature hysteresis characteristics for evaluating whether the carbonate rocks retain a primary or secondary NRM.

Microscopic observations, including SEM and transmission electron microscopy, can greatly facilitate diagnosis of remagnetization in carbonate rocks [*Suk et al.*, 1990a, 1990b, 1991; *Weil and Van der Voo*, 2002; *Huang et al.*, 2015c]. We have observed large amounts of magnetite in carbonate rocks that are pseudomorphs after (sub)euhedral and framboidal pyrite, strongly indicating that this magnetite has an authigenic origin formed during the oxidation of diagenetic pyrite (Figures 4, 5, and 10). SEM observations have also shown that these authigenic magnetite have a heterogeneous texture with pyrite, calcite, and other minerals or voids inside their crystals (Figures 4, 5, and 10), which may explain the rock magnetic behavior of authigenic magnetite that is distinct from that of stoichiometric magnetite. We also have detected rutile pseudomorphic after titanomagnetite (Figures 4, 5, and 10), indicating reductive dissolution of detrital titanomagnetite during diagenesis. Although some detrital titanomagnetite grains survive diagenetic alteration in the Zongshan carbonate rocks, the overwhelming abundance of authigenic magnetite within these specimens challenges the interpretation that a primary NRM can be isolated in these rocks (Figure 4). SEM observations have also confirmed that detrital magnetite is the dominant magnetic carrier and diagenetic pyrite is not oxidized in the fresh Wölong volcaniclastic specimens (Figure 5). The weathered specimens, however, appear to have suffered the same oxidation as the carbonate rocks, with large amounts of authigenic magnetite formed after pyrite (Figure 5). Thus, SEM observations have helped us conclude that dissolution of detrital magnetite and oxidation of iron sulfides to magnetite are the principal remagnetization mechanisms in the Tibetan Himalayan carbonate rocks. Therefore, electron microscopy can provide independent constraints on textural relationships and diagenetic conditions of magnetic minerals and is thus a powerful tool for recognizing remagnetization.

6. Conclusions

The Jurassic to Paleogene strata of the Tibetan Himalaya, mainly composed of carbonate and clastic rocks, were deposited on the northern passive margin of the Indian subcontinent. In this paper, we applied multiple rock magnetic measurements, SEM observations, and EDS analysis on the carbonate and volcaniclastic specimens from these unmetamorphosed strata exposed in the Tingri and Gamba areas. Comprehensive rock magnetic experiments indicate that the dominant magnetic carrier in the carbonate rocks is magnetite, with properties distinguished by wasp-waisted hysteresis loops, hysteresis parameters that plot near or along the SP + SD/PSD mixing curves on the Day plot, suppressed Verwey transitions, an unimodal size distribution of the SP particles with peaks at ~10 nm in diameter, extremely fine grain sizes with 64–92% of ZFC LTSIRM lost at room temperature, and strong frequency dependence of magnetic susceptibility. The magnetic carrier in the volcaniclastic sandstones is also magnetite, but the rock magnetic behavior is distinctly different: pot-bellied hysteresis loops, hysteresis parameters that plot near the SD + MD mixing curves on the Day plot, and clear Verwey transitions. SEM observations and EDS analysis indicate that authigenic magnetite pseudomorphic after iron sulfide is abundant in the carbonate rocks, whereas detrital magnetite that survived diagenetic alteration is rarely found. In contrast, the volcaniclastic sandstones contain large amounts of detrital magnetite with pyrite rarely oxidized to magnetite in fresh specimens. Our rock magnetic and petrographic investigations provide independent constraints on the origin of the NRM retained in these rocks: the Jurassic to Paleogene Tibetan Himalayan carbonate rocks are pervasively remagnetized, whereas the Lower Cretaceous volcaniclastic rocks retain a primary NRM. Remagnetization of the carbonate rocks is probably induced by reductive dissolution of detrital magnetite and oxidation of early diagenetic iron sulfides (i.e., pyrite) to nonstoichiometric magnetite. We infer that these processes were assisted by fluids (either internally buffered or externally derived) before or shortly after the onset of the India-Asia collision. Our work demonstrates that room temperature hysteresis properties, low-temperature hysteresis, RTSIRM, LTSIRM, and AC susceptibility, as well as petrographic observations, are reliable criteria for diagnosing remagnetization in carbonate rocks. We argue that thorough rock magnetic and petrographic studies are prerequisites for paleomagnetic studies throughout southern Tibet and everywhere in general.

Acknowledgments

Data to support this article are available in supporting information Tables S1–S5. This project was funded by the Netherlands Organization for Scientific Research (NWO) with a Rubicon grant (825.15.016) to W.H. The first author was also supported by a visiting research fellowship from the Institute for Rock Magnetism (IRM) at the University of Minnesota, which is funded by the Instruments and Facilities program of NSF. We thank Peter W. Reiners for discussion and Peter A. Solheid at the IRM for laboratory assistance. D.J.J.v.H. was funded through ERC Starting Grant 306810 (SINK) and NWO VIDI grant 864.11.004. We are also grateful to Kenneth P. Kodama and an anonymous reviewer for their constructive comments which have greatly improved the manuscript.

References

Abrajevitch, A., and K. Kodama (2009), Biochemical vs. detrital mechanism of remanence acquisition in marine carbonates: A lesson from the K-T boundary interval, *Earth Planet. Sci. Lett.*, *286*(1), 269–277.

Appel, E., R. Müller, and R. Widder (1991), Paleomagnetic results from the Tibetan Sedimentary Series of the Manang area (north central Nepal), *Geophys. J. Int.*, *104*(2), 255–266.

Appel, E., H. Li, A. Patzelt, and J. Wang (1998), Palaeomagnetic results from late Cretaceous and early Tertiary limestones from Tingri area, southern Tibet, China, *J. Nepal Geol. Soc.*, *18*, 113–124.

Appel, E., C. Crouzet, and E. Schill (2012), Pyrrhotite remagnetizations in the Himalaya: A review, *Geol. Soc. Lond. Spec. Publ.*, *371*(1), 163–180.

Aubourg, C., J.-P. Pozzi, and M. Kars (2012), Burial, claystones remagnetization and some consequences for magnetostratigraphy, *Geol. Soc. Lond. Spec. Publ.*, *371*(1), 181–188.

Besse, J., V. Courtillot, J. P. Pozzi, M. Westphal, and Y. X. Zhou (1984), Paleomagnetic estimates of crustal shortening in the Himalayan thrusts and Zangbo suture, *Nature*, *311*, 621–626.

Chang, L., M. Winklhofer, A. P. Roberts, D. Heslop, F. Florindo, M. J. Dekkers, W. Krijgsman, K. Kodama, and Y. Yamamoto (2013), Low-temperature magnetic properties of pelagic carbonates: Oxidation of biogenic magnetite and identification of magnetosome chains, *J. Geophys. Res. Solid Earth*, *118*, 6049–6065, doi:10.1002/2013JB010381.

Channell, J., and C. McCabe (1994), Comparison of magnetic hysteresis parameters of unremagnetized and remagnetized limestones, *J. Geophys. Res.*, *99*(B3), 4613–4623, doi:10.1029/4693JB02578.

Crouzet, C., H. Stang, E. Appel, E. Schill, and P. Gautam (2001), Detailed analysis of successive pTRMs carried by pyrrhotite in Himalayan metacarbonates: an example from Hidden Valley, Central Nepal, *Geophys. J. Int.*, *146*(3), 607–618.

Crouzet, C., P. Gautam, E. Schill, and E. Appel (2003), Multicomponent magnetization in western Dolpo (Tethyan Himalaya, Nepal): Tectonic implications, *Tectonophysics*, *377*(1), 179–196.

Day, R., M. Fuller, and V. Schmidt (1977), Hysteresis properties of titanomagnetites: Grain-size and compositional dependence, *Phys. Earth Planet. In.*, *13*(4), 260–267.

DeCelles, P., P. Kapp, G. Gehrels, and L. Ding (2014), Paleocene-Eocene foreland basin evolution in the Himalaya of southern Tibet and Nepal: Implications for the age of initial India-Asia collision, *Tectonics*, *33*, 824–849, doi:10.1002/2014TC003522.

DeCelles, P. G., D. M. Robinson, and G. Zandt (2002), Implications of shortening in the Himalayan fold-thrust belt for uplift of the Tibetan Plateau, *Tectonics*, *21*(6), 1062, doi:10.1029/2001TC001322.

Dekkers, M. J. (2012), End-member modelling as an aid to diagnose remagnetization: A brief review, *Geol. Soc. Lond. Spec. Publ.*, *371*(1), 253–269.

Dinarès-Turell, J., and J. Garcia-Senz (2000), Remagnetization of Lower Cretaceous limestones from the southern Pyrenees and relation to the Iberian plate geodynamic evolution, *J. Geophys. Res.*, *105*(B8), 19,405–19,418, doi:10.1029/2000JB900136.

Ding, L., M. Qasim, I. A. Jadoon, M. A. Khan, Q. Xu, F. Cai, H. Wang, U. Baral, and Y. Yue (2016), The India–Asia collision in north Pakistan: Insight from the U–Pb detrital zircon provenance of Cenozoic foreland basin, *Earth Planet. Sci. Lett.*, *455*, 49–61.

Du, X., X. Chen, C. Wang, Y. Wei, L. Yalin, and L. Jansa (2015), Geochemistry and detrital zircon U-Pb dating of Lower Cretaceous volcaniclastics in the Babazhadong section, Northern Tethyan Himalaya: Implications for the breakup of Eastern Gondwana, *Cretaceous Res.*, *52*, 127–137.

Dunlop, D. J. (2002), Theory and application of the Day plot (M_{rs}/M_s versus H_{cr}/H_c): 2. Application to data for rocks, sediments, and soils, *J. Geophys. Res.*, *107*(B3), 2057, doi:10.1029/2001JB000487.

Dunlop, D. J., and Ö. Ödemir (1997), *Rock Magnetism: Fundamentals and Frontiers*, 573 pp., Cambridge Univ. Press, Cambridge.

Elmore, R. D., A. R. Muxworthy, and M. Aldana (2012), Remagnetization and chemical alteration of sedimentary rocks, *Geol. Soc. Lond. Spec. Publ.*, *371*(1), 1–21.

Fabian, K. (2003), Some additional parameters to estimate domain state from isothermal magnetization measurements, *Earth Planet. Sci. Lett.*, *213*(3), 337–345.

Fabian, K., and T. Dobeneck (1997), Isothermal magnetization of samples with stable Preisach function: A survey of hysteresis, remanence, and rock magnetic parameters, *J. Geophys. Res.*, *102*(B8), 17,659–17,677, doi:10.1029/97JB01051.

Ferry, J. M. (1981), Petrology of graphitic sulfide-rich schists from south-central Maine: An example of desulfidation during prograde regional metamorphism, *Am. Mineral.*, *66*(9–10), 908–930.

Garzanti, E. (1999), Stratigraphy and sedimentary history of the Nepal Tethys Himalaya passive margin, *J. Asian Earth Sci.*, *17*(5), 805–827.

Gong, Z., D. van Hinsbergen, and M. Dekkers (2009), Diachronous pervasive remagnetization in northern Iberian basins during Cretaceous rotation and extension, *Earth Planet. Sci. Lett.*, *284*(3), 292–301.

Hall, A. (1986), Pyrite-pyrrhotine redox reactions in nature, *Mineral. Mag.*, *50*(6), 223–229.

Han, Z., X. Hu, J. Li, and E. Garzanti (2016), Jurassic carbonate microfacies and relative sea-level changes in the Tethys Himalaya (southern Tibet), *Palaeogeogr. Palaeoclimatol. Palaeoecol.*, *456*, 1–20.

Hodges, K. V. (2000), Tectonics of the Himalaya and southern Tibet from two perspectives, *Geol. Soc. Am. Bull.*, *112*, 324–350.

Hu, X., L. Jansa, L. Chen, W. L. Griffin, S. Y. O'Reilly, and J. Wang (2010), Provenance of Lower Cretaceous Wölong volcaniclastics in the Tibetan Tethyan Himalaya: Implications for the final breakup of eastern Gondwana, *Sediment. Geol.*, *223*(3), 193–205.

Hu, X., H. D. Sinclair, J. Wang, H. Jiang, and F. Wu (2012), Late Cretaceous-Palaeogene stratigraphic and basin evolution in the Zhepure Mountain of southern Tibet: Implications for the timing of India-Asia initial collision, *Basin Res.*, *24*(5), 520–543.

Hu, X., E. Garzanti, T. Moore, and I. Raffi (2015a), Direct stratigraphic dating of India-Asia collision onset at the Selandian (middle Paleocene, 59 ± 1 Ma), *Geology*, *43*(10), 859–862.

Hu, X., J. Wang, M. BouDagher-Fadel, E. Garzanti, and W. An (2015b), New insights into the timing of the India–Asia collision from the Paleogene Quxia and Jialazi formations of the Xigaze forearc basin, South Tibet, *Gondw. Res.*, *32*, 76–92.

Hu, X., E. Garzanti, J. Wang, W. Huang, W. An, and A. Webb (2016a), The timing of India-Asia collision onset—Facts, theories, controversies, *Earth Sci. Rev.*, *160*, 264–299.

Hu, X., J. Wang, M. BouDagher-Fadel, E. Garzanti, and W. An (2016b), New insights into the timing of the India–Asia collision from the Paleogene Quxia and Jialazi formations of the Xigaze forearc basin, South Tibet, *Gondw. Res.*, *32*, 76–92.

Hu, X., J. Wang, W. An, E. Garzanti, and J. Li (2017), Constraining the timing of the India-Asia continental collision by the sedimentary record, *Sci. China Earth Sci.*, 1–23.

Huang, W., G. Dupont-Nivet, P. C. Lippert, D. J. J. van Hinsbergen, and E. Hallot (2013), Inclination shallowing in Eocene Linzizong sedimentary rocks from Southern Tibet: Correction, possible causes and implications for reconstructing the India–Asia collision, *Geophys. J. Int.*, *194*(3), 1390–1411.

Huang, W., G. Dupont-Nivet, P. C. Lippert, D. J. J. van Hinsbergen, M. J. Dekkers, R. Waldrip, M. Ganerød, X. Li, Z. Guo, and P. Kapp (2015a), What was the Paleogene latitude of the Lhasa terrane? A reassessment of the geochronology and paleomagnetism of Linzizong volcanic rocks (Linzhou Basin, Tibet), *Tectonics*, *34*, 594–622, doi:10.1002/2014TC003787.

Huang, W., G. Dupont-Nivet, P. C. Lippert, D. J. J. van Hinsbergen, M. J. Dekkers, Z. Guo, R. Waldrip, X. Li, X. Zhang, and D. Liu (2015b), Can a primary remanence be retrieved from partially remagnetized Eocence volcanic rocks in the Nanmulin Basin (southern Tibet) to date the India-Asia collision?, *J. Geophys. Res. Solid Earth*, *120*, 42–66, doi:10.1002/2014JB011599.

Huang, W., et al. (2015c), Paleolatitudes of the Tibetan Himalaya from primary and secondary magnetizations of Jurassic to Lower Cretaceous sedimentary rocks, *Geochem. Geophys. Geosyst.*, *16*, 77–100, doi:10.1002/2014GC005624.

Huang, W., D. J. J. van Hinsbergen, P. C. Lippert, Z. Guo, and G. Dupont-Nivet (2015d), Paleomagnetic tests of tectonic reconstructions of the India-Asia collision zone, *Geophys. Res. Lett.*, *42*, 2642–2649, doi:10.1002/2015GL063749.

Huang, W., P. C. Lippert, M. J. Dekkers, M. J. Jackson, Y. Zhang, J. Li, Z. Guo, P. Kapp, and D. J. J. van Hinsbergen (2017), Remagnetization of the Paleogene Tibetan Himalayan carbonate rocks in the Gamba area: Implications for reconstructing the lower plate in the India-Asia collision, *J. Geophys. Res. Solid Earth*, *122*, 808–825, doi:10.1002/2016JB013662.

Jackson, M. (1990), Diagenetic sources of stable remanence in remagnetized Paleozoic cratonic carbonates: A rock magnetic study, *J. Geophys. Res.*, *95*(B3), 2753–2761, doi:10.1029/JB2095iB2703p02753.

Jackson, M., and N. L. Swanson-Hysell (2012), Rock magnetism of remagnetized carbonate rocks: Another look, *Geol. Soc. Lond. Spec. Publ.*, *371*(1), 229–251.

Jackson, M., and H.-U. Worm (2001), Anomalous unblocking temperatures, viscosity and frequency-dependent susceptibility in the chemically-remagnetized Trenton limestone, *Phys. Earth Planet. In.*, *126*(1), 27–42.

Jackson, M., C. McCabe, M. M. Ballard, and R. Van der Voo (1988), Magnetite authigenesis and diagenetic paleotemperatures across the northern Appalachian basin, *Geology*, *16*(7), 592–595.

Jadoul, F., F. Berra, and E. Garzanti (1998), The Tethys Himalayan passive margin from Late Triassic to Early Cretaceous (South Tibet), *J. Asian Earth Sci.*, *16*(2), 173–194.

Karlin, R., and S. Levi (1983), Diagenesis of magnetic minerals in recent haemipelagic sediments, *Nature*, *303*(5915), 327–330.

Katz, B., R. D. Elmore, M. Cogoini, M. H. Engel, and S. Ferry (2000), Associations between burial diagenesis of smectite, chemical remagnetization, and magnetite authigenesis in the Vocontian trough, SE France, *J. Geophys. Res.*, *105*(B1), 851–868, doi:10.1029/1999JB900309.

Kent, D. V. (1985), Thermoviscous remagnetization in some Appalachian limestones, *Geophys. Res. Lett.*, *12*(12), 805–808, doi:10.1029/GL1012i1012p00805.

Klootwijk, C. T. (1984), A review of Indian Phanerozoic paleomagnetism: Implications for the Indo-Asia collision, *Tectonophysics*, *105*, 331–353.

Klootwijk, C. T., and D. K. Bingham (1980), The extent of Greater India: III. Paleomagnetic data from the Tibetan Sedimentary series, Thakkhola region, Nepal Himalaya, *Earth Planet. Sci. Lett.*, *51*(2), 381–405.

Klootwijk, C. T., S. Shah, J. Gergan, M. L. Sharma, B. Tirkey, and B. Gupta (1983), A paleomagnetic reconnaissance of Kashmir, northwestern Himalaya, India, *Earth Planet. Sci. Lett.*, *63*(2), 305–324.

Kodama, K. P. (2009), Simplification of the anisotropy-based inclination correction technique for magnetite- and haematite-bearing rocks: A case study for the Carboniferous Glenshaw and Mauch Chunk Formations, North America, *Geophys. J. Int.*, *176*(2), 467–477.

Kodama, K. P. (2012), *Paleomagnetism of Sedimentary Rocks: Process and Interpretation*, 157 pp., Wiley-Blackwell, Oxford.

Lanci, L., and D. V. Kent (2006), Meteoric smoke fallout revealed by superparamagnetism in Greenland ice, *Geophys. Res. Lett.*, *33*, L13308, doi:10.1029/2006GL026480.

Larrasoaña, J. C., A. P. Roberts, R. J. Musgrave, E. Gràcia, E. Piñero, M. Vega, and F. Martínez-Ruiz (2007), Diagenetic formation of greigite and pyrrhotite in gas hydrate marine sedimentary systems, *Earth Planet. Sci. Lett.*, *261*(3), 350–366.

Li, J., and X. Hu (2013), Tectonic subsidence analysis of Late Triassic-Paleogene strata in Tingri area, Tibetan Tethyan Himalaya and evolution of sedimentary basins, *Acta Geophys. Sin.*, *29*(11), 3843–3851.

Li, J., X. Hu, E. Garzanti, W. An, and J. Wang (2015), Paleogene carbonate microfacies and sandstone provenance (Gamba area, South Tibet): Stratigraphic response to initial India–Asia continental collision, *J. Asian Earth Sci.*, *104*, 39–54.

Li, Z., L. Ding, P. C. Lippert, P. Song, Y. Yue, and D. J. van Hinsbergen (2016), Paleomagnetic constraints on the Mesozoic drift of the Lhasa terrane (Tibet) from Gondwana to Eurasia, *Geology*, *44*(9), 727–730.

Liebke, U., E. Appel, L. Ding, and Q. Zhang (2013), Age constraints on the India–Asia collision derived from secondary remanences of Tethyan Himalayan sediments from the Tingri area, *J. Asian Earth Sci.*, *62*, 329–340.

Lippert, P. C., D. J. J. van Hinsbergen, and G. Dupont-Nivet (2014), The Early Cretaceous to Present latitude of the central Lhasa-plano (Tibet): A paleomagnetic synthesis with implications for Cenozoic tectonics, paleogeography and climate of Asia, in *Towards an Improved Understanding of Uplift Mechanisms and the Elevation History of the Tibetan Plateau*, edited by J. S. Nie, G. D. Hoke, and B. K. Horton, *Geol. Soc. Am. Spec. Pap.*, *507*, 1–21.

Liu, Q., C. Deng, Y. Yu, J. Torrent, M. J. Jackson, S. K. Banerjee, and R. Zhu (2005), Temperature dependence of magnetic susceptibility in an argon environment: Implications for pedogenesis of Chinese loess/palaeosols, *Geophys. J. Int.*, *161*(1), 102–112.

Long, S., N. McQuarrie, T. Tobgay, and D. Grujic (2011), Geometry and crustal shortening of the Himalayan fold-thrust belt, eastern and central Bhutan, *Bull. Geol. Soc. Am.*, *123*(7–8), 1427.

Ma, Y., T. Yang, W. Bian, J. Jin, S. Zhang, H. Wu, and H. Li (2016), Early Cretaceous paleomagnetic and geochronologic results from the Tethyan Himalaya: Insights into the Neotethyan paleogeography and the India–Asia collision, *Sci. Rep.*, *6*, 21605.

Maloof, A. C., R. E. Kopp, J. P. Grotzinger, D. A. Fike, T. Bosak, H. Vali, P. M. Poussart, B. P. Weiss, and J. L. Kirschvink (2007), Sedimentary iron cycling and the origin and preservation of magnetization in platform carbonate muds, Andros Island, Bahamas, *Earth Planet. Sci. Lett.*, *259*(3), 581–598.

McCabe, C., and R. D. Elmore (1989), The occurrence and origin of Late Paleozoic remagnetization in the sedimentary rocks of North America, *Rev. Geophys.*, *27*(4), 471–494, doi:10.1029/JB1094iB1008p10429.

McCabe, C., R. Van der Voo, D. R. Peacor, C. R. Scotese, and R. Freeman (1983), Diagenetic magnetite carries ancient yet secondary remanence in some Paleozoic sedimentary carbonates, *Geology*, *11*(4), 221–223.

Moskowitz, B. M., R. B. Frankel, D. A. Bazylinski, H. W. Jannasch, and D. R. Lovley (1989), A comparison of magnetite particles produced anaerobically by magnetotactic and dissimilatory iron-reducing bacteria, *Geophys. Res. Lett.*, *16*(7), 665–668, doi:10.1029/GL016i007p00665.

Moskowitz, B. M., R. B. Frankel, and D. A. Bazylinski (1993), Rock magnetic criteria for the detection of biogenic magnetite, *Earth Planet. Sci. Lett.*, *120*(3–4), 283–300.

Najman, Y., E. Appel, M. Boudagher-Fadel, P. Bown, A. Carter, E. Garzanti, L. Godin, J. Han, U. Liebke, and G. Oliver (2010), Timing of India-Asia collision: Geological, biostratigraphic, and palaeomagnetic constraints, *J. Geophys. Res.*, *115*, B12416, doi:10.1029/2010JB007673.

Néel, L. (1949), Théorie du traînage magnétique des ferromagnétiques en grains fins avec applications aux terres cuites, *Ann. Geophys.*, *5*(2), 99–136.

Oldfield, F., A. Hunt, M. Jones, R. Chesteri, J. Dearingi, L. Olsson, and J. Prosperoll (1985), Magnetic differentiation of atmospheric dusts, *Nature*, *317*, 10.

Orme, D. A., B. Carrapa, and P. Kapp (2014), Sedimentology, provenance and geochronology of the upper Cretaceous–lower Eocene western Xigaze forearc basin, southern Tibet, *Basin Res.*, 1–25, doi:10.1111/bre.12080.

Özdemir, Ö., and D. J. Dunlop (2010), Hallmarks of maghemitization in low-temperature remanence cycling of partially oxidized magnetite nanoparticles, *J. Geophys. Res.*, *115*, B02101, doi:10.1029/02009JB006756.

Özdemir, Ö., D. J. Dunlop, and B. M. Moskowitz (1993), The effect of oxidation on the Verwey transition in magnetite, *Geophys. Res. Lett.*, *20*(16), 1671–1674, doi:10.1029/1693GL01483.

Özdemir, Ö., D. J. Dunlop, and T. S. Berquo (2008), Morin transition in hematite: Size dependence and thermal hysteresis, *Geochem. Geophys. Geosyst.*, *9*, Q10Z01, doi:10.1029/2008GC002110.

Patzelt, A., H. Li, J. Wang, and E. Appel (1996), Palaeomagnetism of Cretaceous to Tertiary sediments from southern Tibet: Evidence for the extent of the northern margin of India prior to the collision with Eurasia, *Tectonophysics*, *259*, 259–284.

Powell, C. M., and P. Conaghan (1973), Plate tectonics and the Himalayas, *Earth Planet. Sci. Lett.*, *20*(1), 1–12.

Ran, B., C. Wang, X. Zhao, Y. Li, J. Meng, K. Cao, and P. Wang (2012), Dimension of Greater India in the early Mesozoic: Paleomagnetic constraints from Triassic sediments in the Tethyan Himalaya, *J. Asian Earth Sci.*, *53*, 15–24.

Rivas, J., J. Zamarro, E. Martin, and C. Pereira (1981), Simple approximation for magnetization curves and hysteresis loops, *IEEE Trans. Magn.*, *17*(4), 1498–1502.

Roberts, A. P., Y. Cui, and K. L. Verosub (1995), Wasp-waisted hysteresis loops: Mineral magnetic characteristics and discrimination of components in mixed magnetic systems, *J. Geophys. Res.*, *100*(B9), 17,909–17,924, doi:10.1029/17995JB00672.

Roberts, A. P., F. Florindo, L. Chang, D. Heslop, L. Jovane, and J. C. Larrasoaña (2013), Magnetic properties of pelagic marine carbonates, *Earth Sci. Rev.*, *127*, 111–139.

Rochette, P. (1987), Metamorphic control of the magnetic mineralogy of black shales in the Swiss Alps: Toward the use of "magnetic isograds", *Earth Planet. Sci. Lett.*, *84*(4), 446–456.

Schill, E., E. Appel, and P. Gautam (2002), Towards pyrrhotite/magnetite geothermometry in low-grade metamorphic carbonates of the Tethyan Himalayas (Shiar Khola, Central Nepal), *J. Asian Earth Sci.*, *20*(3), 195–201.

Smirnov, A. V., and J. A. Tarduno (2001), Estimating superparamagnetism in marine sediments with the time dependency of coercivity of remanence, *J. Geophys. Res.*, *106*(B8), 16,135–16,143, doi:10.1029/12001JB000152.

Sparks, N., S. Mann, D. Bazylinski, D. Lovley, H. Jannasch, and R. B. Frankel (1990), Structure and morphology of magnetite anaerobically-produced by a marine magnetotactic bacterium and a dissimilatory iron-reducing bacterium, *Earth Planet. Sci. Lett.*, *98*(1), 14–22.

Suk, D., D. Peacor, and R. Van der Voo (1990a), Replacement of pyrite framboids by magnetite in limestone and implications for palaeomagnetism, *Nature*, *345*(6276), 611–613.

Suk, D., R. Van der Voo, and D. R. Peacor (1990b), Scanning and transmission electron microscope observations of magnetite and other iron phases in Ordovician carbonates from east Tennessee, *J. Geophys. Res.*, *95*(B8), 12,327–12,336, doi:10.1029/JB12095iB12308p12327.

Suk, D., R. Van der Voo, and D. R. Peacor (1991), SEM/STEM observations of magnetite in carbonates of eastern North America: Evidence for chemical remagnettzation during the Alleghenian Orogeny, *Geophys. Res. Lett.*, *18*(5), 939–942, doi:10.1029/1091GL00916.

Suk, D., R. Van Der Voo, and D. R. Peacor (1993), Origin of magnetite responsible for remagnetization of early Paleozoic limestones of New York State, *J. Geophys. Res.*, *98*(B1), 419–434, doi:10.1029/1092JB01323.

Tarduno, J. A., and M. Myers (1994), A primary magnetization fingerprint from the Cretaceous Laytonville Limestone: Further evidence for rapid oceanic plate velocities, *J. Geophys. Res.*, *99*(B11), 21,691–21,703, doi:10.1029/21694JB01939.

Tauxe, L., and D. V. Kent (2004), A simplified statistical model for the geomagnetic field and the detection of shallow bias in paleomagnetic inclinations: Was the ancient magnetic field dipolar, in *Timescales of the Paleomagnetic Field, Geophys. Monogr. Ser.*, vol. 145, edited by J. E. T. Channell et al., pp. 101–115, AGU, Washington, D. C., doi:10.1029/145GM08.

Tauxe, L., T. Mullender, and T. Pick (1996), Potbellies, wasp-waists, and superparamagnetism in magnetic hysteresis, *J. Geophys. Res.*, *101*(B1), 571–583, doi:10.1029/1095JB03041.

Tohver, E., A. Weil, J. Solum, and C. Hall (2008), Direct dating of carbonate remagnetization by $^{40}Ar/^{39}Ar$ analysis of the smectite–illite transformation, *Earth Planet. Sci. Lett.*, *274*(3), 524–530.

Tong, Y., Z. Y. Yang, L. Zheng, T. S. Yang, L. F. Shi, Z. M. Sun, and J. L. Pei (2008), Early Paleocene paleomagnetic results from southern Tibet, and tectonic implications, *Int. Geol. Rev.*, *50*(6), 546–562.

Torsvik, T. H., T. S. Paulsen, N. C. Hughes, P. M. Myrow, and M. GANERØD (2009), The Tethyan Himalaya: Palaeogeographical and tectonic constraints from Ordovician palaeomagnetic data, *J. Geol. Soc. London*, *166*(4), 679–687.

Torsvik, T. H., R. Van der Voo, U. Preeden, C. Mac Niocaill, B. Steinberger, P. V. Doubrovine, D. J. J. van Hinsbergen, M. Domeier, C. Gaina, and E. Tohver (2012), Phanerozoic polar wander, palaeogeography and dynamics, *Earth Sci. Rev.*, *114*(3), 325–368.

van der Voo, R., and T. H. Torsvik (2012), The history of remagnetization of sedimentary rocks: Deceptions, developments and discoveries, *Geol. Soc. Lond. Spec. Publ.*, *371*(1), 23–53.

Van der Voo, R., J. A. Stamakos, and J. M. Pares (1997), Kinematic constraints on thrust-belt curvature from syndeformational magnetizations in the Lagos del Valle syncline in the Cantabrian arc, Spain, *J. Geophys. Res.*, *102*(B5), 10,105–10,119, doi:10.1029/10197JB00263.

van Hinsbergen, D. J., B. Steinberger, P. V. Doubrovine, and R. Gassmöller (2011), Acceleration and deceleration of India-Asia convergence since the Cretaceous: Roles of mantle plumes and continental collision, *J. Geophys. Res.*, *116*, B06101, doi:10.1029/02010JB008051.

van Hinsbergen, D. J. J., P. C. Lippert, G. Dupont-Nivet, N. McQuarrie, P. V. Doubrovine, W. Spakman, and T. H. Torsvik (2012), Greater India Basin hypothesis and a two-stage Cenozoic collision between India and Asia, *Proc. Natl. Acad. Sci.*, *109*(20), 7659–7664.

Wan, X. Q., L. F. Jansa, and M. Sarti (2002), Cretaceous and Paleogene boundary strata in southern Tibet and their implication for the India-Eurasia collision, *Lethaia*, *35*(2), 131–146.

Wang, J., X. Hu, L. Jansa, and Z. Huang (2011), Provenance of the Upper Cretaceous–Eocene deep-water sandstones in Sangdanlin, southern Tibet: Constraints on the timing of initial India-Asia collision, *J. Geol.*, *119*(3), 293–309.

Weil, A. B., and R. Van der Voo (2002), Insights into the mechanism for orogen-related carbonate remagnetization from growth of authigenic Fe-oxide: A scanning electron microscopy and rock magnetic study of Devonian carbonates from northern Spain, *J. Geophys. Res.*, *107*(B4), EPM 1-1–EPM 1-14, doi:10.1029/2001JB000200.

Wendler, I., J. Wendler, K.-U. Gräfe, J. Lehmann, and H. Willems (2009), Turonian to Santonian carbon isotope data from the Tethys Himalaya, southern Tibet, *Cretaceous Res.*, *30*(4), 961–979.

Willems, H., Z. Zhou, B. Zhang, and K.-U. Grafe (1996), Stratigraphy of the Upper Cretaceous and lower Tertiary strata in the Tethyan Himalayans of Tibet (Tingri area, China), *Geogr. Rundsch.*, *85*, 723–745.

Worm, H. U., and M. Jackson (1999), The superparamagnetism of Yucca Mountain tuff, *J. Geophys. Res.*, *104*(B11), 25,415–25,425, doi:10.1029/21999JB900285.

Yang, T., Y. Ma, W. Bian, J. Jin, S. Zhang, H. Wu, H. Li, Z. Yang, and J. Ding (2015), Paleomagnetic results from the Early Cretaceous Lakang Formation lavas: Constraints on the paleolatitude of the Tethyan Himalaya and the India–Asia collision, *Earth Planet. Sci. Lett.*, *428*, 120–133.

Yi, Z., B. Huang, J. Chen, L. Chen, and H. Wang (2011), Paleomagnetism of early Paleogene marine sediments in southern Tibet, China: Implications to onset of the India-Asia collision and size of Greater India, *Earth Planet. Sci. Lett.*, *309*(1), 153–165.

Yin, A., and M. T. Harrison (2000), Geologic evolution of the Himalayan-Tibetan orogen, *Annu. Rev. Earth Planet. Sci.*, *28*, 211–280.

Zegers, T., M. Dekkers, and S. Bailly (2003), Late Carboniferous to Permian remagnetization of Devonian limestones in the Ardennes: Role of temperature, fluids, and deformation, *J. Geophys. Res.*, *108*(B7), 2357, doi:10.1029/2002JB002213.

Zhu, B., W. S. Kidd, D. B. Rowley, B. S. Currie, and N. Shafique (2005), Age of initiation of the India-Asia collision in the east-central Himalaya, *J. Geol.*, *113*(3), 265–285.

Zwing, A., J. Matzka, V. Bachtadse, and H. Soffel (2005), Rock magnetic properties of remagnetized Palaeozoic clastic and carbonate rocks from the NE Rhenish massif, Germany, *Geophys. J. Int.*, *160*(2), 477–486.

Zwing, A., N. Clauer, N. Liewig, and V. Bachtadse (2009), Identification of remagnetization processes in Paleozoic sedimentary rocks of the northeast Rhenish Massif in Germany by K-Ar dating and REE tracing of authigenic illite and Fe oxides, *J. Geophys. Res.*, *114*, B06104, doi:10.1029/2008JB006137.